UNIVERSITY OF CALIFORNIA
RIVERSIDE

Pre-Erupted Water Concentrations in Erta Ale Lavas and Gulf of Aden Glasses from the East African Rift

A Thesis submitted in partial satisfaction
of the requirements for the degree of

Master of Science

in

Geological Sciences

by

Sara Laurene Scoggins

June 2022

Thesis Committee:
Dr. Maryjo Brounce, Chairperson
Dr. Heather A. Ford
Dr. Andrey Bekker

The Thesis of Sara Laurene Scoggins is approved:

_____

_____

_____

Committee Chairperson

University of California, Riverside

ACKNOWLEDGEMENTS

I would first like to thank my thesis advisor Dr. Maryjo Brounce, who expertly guided me through my graduate education, and who shared the excitement of petrology and research with me throughout my time at the University of California Riverside. Her motivation, sincerity, and passion has greatly inspired and motivated me. I am extremely grateful to have been given the opportunity to work and study under her guidance.

Secondly, I would like to thank the support from NSF GeoPRISMS as the NSF EAR1849700 grant allowed me to be a part of this amazing research opportunity. I would also like to thank Tobias Fischer at the University of New Mexico for providing the samples that allowed me to partake in this research as well as the UCLA Department of Earth, Planetary, and Space Sciences for assistance and access to the UCLA microprobe.

Lastly, I would also like to thank my friends and family for being a great support system through my years of education, and I would also like to specifically thank my mom. She has been my number one supporter for my entire life, and without her I would not be the person I am today. Her sacrifices and dedication have allowed me to live my dreams, and without her this would not have been possible.

ABSTRACT OF THE THESIS

Pre-Erupted Water Concentrations in Erta Ale Lavas and Gulf of Aden Glasses from the East African Rift

by

Sara Laurene Scoggins

Master of Science, Graduate Program in Geological Sciences
University of California Riverside, June 2022
Dr. Maryjo Brounce, Chairperson

The compositions of lavas in East African Rift suggest that the upper mantle temperatures in this region are high (~1360-1490°C), however, seismic wave speeds are very low, which if due to elevated mantle temperatures alone, would require mantle potential temperatures >1700°C. This suggests a significant role for H_2O, CO_2, or melt in the mantle under the East African Rift. The volatile contents of submarine glasses from the Gulf of Aden are unknown but are key to constraining H_2O contents in the mantle in this area. The radiogenic isotope (Sr-Nd-Hf-Pb) compositions of these glasses point to three distinct mantle sources for the lavas erupted along the East African Rift: the depleted upper mantle, the Afar mantle plume, and the Pan-African lithosphere. We present major and volatile element compositions and $S^{6+}/\Sigma S$ of glassy melt inclusions and their phenocryst hosts from Erta Ale, and S, H_2O, $S^{6+}/\Sigma S$, and $Fe^{3+}/\Sigma Fe$ of selected Gulf of Aden glasses to constrain primary melt and mantle source H_2O and melt fractions along the rift. Erta Ale inclusions are basaltic, have 0.05-0.4 wt% H_2O, and ~0.16

$Fe^{3+}/\Sigma Fe$. Gulf of Aden glasses are basaltic, have ~0.16 $Fe^{3+}/\Sigma Fe$, and are divided into groups based on K_2O. "Low K_2O" glasses have 0.15-0.36 wt% H_2O, "Medium K_2O" have 0.05-0.22 wt% H_2O, and "High K_2O" have 0.84 wt% H_2O. We calculate primary melt compositions for samples with MgO > 8 wt% and find that Gulf of Aden samples represent 7-10% melts of the mantle. Assuming a H_2O content for the solid depleted upper mantle of 0.012 wt%, our calculated melt fractions, primary melt H_2O contents, and known partition coefficients, we calculate the H_2O of the Pan-African lithosphere (0-0.4 wt%) and the Afar mantle plume (0.06 wt%). These values enable a more nuanced characterization of the geophysical anomaly under the East African Rift.

Table of Contents

Table of Figures

Table of Tables

Introduction

Continental rifting is a primary component of modern plate tectonic cycles. It records the onset on continental fragmentation (Condie & Kröner, 2008) and the progression to the production of new oceanic crust and ocean basins. The East African Rift is one modern, developing example of a continental rift and provides a description of the complexity of this process, including the role that magma may play in promoting extension and the breakup of the lithosphere (Corti, 2012). Despite its importance, the physical mechanisms that drive the initiation and development of continental rifts remain uncertain. The expected magnitudes of the major tectonic forces such as slab pull, asthenospheric drag, and ridge push (Forsyth & Uyeda, 1975) are insufficient to overcome the expected strength of continental lithosphere (Buck, 2004), suggesting that continental lithosphere is weakened prior to rifting. One way this could be accomplished is through the injection of magma or other fluids into the continental lithosphere, and indeed, some continental rifts are associated with significant magmatism at the time of initiation of the rift (e.g., East African Rift and the Ethiopian Flood Basalt Province (Hofmann et al., 1997; Mohr & Zanettin, 1988). The production of this magmatism through mantle melting presents new challenges - continental lithosphere ranges from 40 km to 280 km in thickness (Pasyanos, 2010) and there is significantly lower heat flow beneath continents (a mean value of 64.7 mW m^{-2}) than beneath oceans (a mean value of ~95.9 mW m^{-2}) (Davies, 2013; Jaupart, 2009). Assuming that pre-rifted continental lithosphere is similarly thick, in the absence of any elevated temperatures or H_2O and/or

CO_2 in the mantle under pre-rifted continental lithosphere, one would expect limited extents of melting if generated by decompression. This suggests that magma-assisted continental rifting also requires elevated mantle temperatures and/or easily fused lithologies such as hydrous or carbonated phases.

The East African Rift System is driven by extension and the thinning of the African plate, creating the Main Ethiopian Rift and the eastern and western branches (also referred to as the Albertine and Gregory rifts) of the East African Rift (Figure 1) (Chorowicz, 2005; Scoon, 2018). The Main Ethiopian rift forms a triple junction along with spreading centers in the Red Sea and Gulf of Aden (Figure 1) (Scoon, 2018). The eastern branch of the East African Rift extends 2200 km from the Afar triangle, includes the Main Ethiopian and Kenyan rifts, and ends in the basins of North Tanzania. The western branch extends a distance of 2100 km starting on the border of the Democratic Republic of Congo and Uganda, and extends south through Zambia and into Mozambique (Chorowicz, 2005). There is a third southeastern branch that lies in the Mozambique channel. The major element compositions of relatively unevolved lavas throughout the Ethiopian/Afar triangle suggests moderate thermal anomalies; ~140 °C warmer than ambient upper mantle at the same depth, corresponding to an approximate absolute temperature of 1490°C (Rooney et al., 2012). This is low compared to other large igneous provinces and so-called hot spot lavas, which have temperatures ranging from 1300 °C to 1700 °C (Rooney et al., 2012). A potential temperature of ~1490 °C for the mantle under the East African rift is potentially at odds with present day geophysical observations of the upper mantle. Elevated mantle potential temperatures are expected to

slow seismic wave velocity (Karato & Jung, 2003), and indeed the observed P- and S-wave speeds beneath the East African Rift present one of the most prominent geophysical anomalies in Earth's upper mantle, with seismic wave speeds of δVp~ -6%, δVs~ -4.47% relative to standard Earth models (Figure 2) (Bastow et al., 2008; Emry et al., 2019). If this slowness were due to increased mantle temperatures alone, it would require lavas that record mantle potential temperatures of ~1700 °C (Gallacher et al., 2016) – far in excess of the constraints from lavas described above. This indicates that other characteristics of the mantle under the East African Rift – such as increased H_2O, CO_2, or melt fraction, may play a role in slowing seismic wave speeds, and perhaps in the rifting process itself.

Elevated concentrations of volatile elements (e.g., H_2O and CO_2) in the mantle rock can slow seismic wave speeds through modification of the shear modulus (Karato & Jung, 1998). Additionally, the presence of volatile elements in their oxidized forms (e.g., H_2O and CO_2) can lower the peridotite solidus (Dasgupta & Hirschmann, 2007; Till et al., 2012) allowing for melt generation at higher pressures and/or lower temperatures than ambient upper mantle. For example, the presence of H_2O lowers the peridotite solidus by ~200°C at 3 GPa (Dasgupta & Hirschmann, 2007; Till et al., 2012). The presence of melt in mantle rocks would in turn modify the sheer modulus and lowers seismic wave velocities. The impact of volatiles on seismic wave velocities can thus be two-fold – lowering the sheer modulus by 1) their presence in the mantle rock, and 2) promoting melt generation.

The slowest wave speeds of the geophysical anomaly are centered in the Afar triangle of the East African Rift (Figure 2). Though there are abundant volcanic rocks at

the surface in this region, constraints on the volatile contents on these rocks are somewhat limited because the focus thus far has been on measuring the compositions of lavas erupted to the surface. These lavas are routinely partially to fully degassed of their volatile elements, including H_2O and CO_2, and thus cannot be used to interrogate the volatile contents of the mantle that produces these rocks. Phenocryst-hosted melt inclusions are blebs of magma trapped inside of phenocrysts when the phenocrysts grow at relatively higher pressures than that of eruption at the surface (Figure 3). These can be useful for studies seeking to measure pre- or less-degassed H_2O and CO_2 contents of magmas, because the crystal host acts as a pressurized container during ascent and eruption to the surface, resulting in glassy melt inclusions that can be measured and record the abundance of volatile elements in less degassed magma compositions (Plank et al., 2013; Saal et al., 2002). Plagioclase, olivine, and clinopyroxene-hosted melt inclusions from Nabro and Dabbahu volcanoes, both located in the Afar triangle (Figure 1), point to undegassed H_2O concentrations near 1.3 wt% (Donovan et al., 2018; Field et al., 2012). Olivine hosted melt inclusions from Erta Ale (Figure 1) have lower H_2O and CO_2 contents (~0.1 wt% H_2O; ~200 ppm CO_2) (Field et al., 2012), and a wide range of S contents (~140-1218ppm) (de Moor et al., 2013). On one hand, the low H_2O and CO_2 concentrations of Erta Ale magmas suggest a dry and low carbon mantle source similar to the depleted upper mantle; on the other hand, the higher H_2O contents recorded by melt inclusions from Nabro indicate that there may be variability in the distribution of H_2O in the mantle source of this region.

The volatile contents of submarine glasses from the Gulf of Aden are unknown but are key to determining the possibility of variability in H_2O contents in magmas in this area. The radiogenic isotope (Sr-Nd-Hf-Pb) compositions of these glasses point to three distinct mantle sources that contribute melts that ultimately mix in variable proportions and erupt to form the pillow lavas of the Gulf of Aden and the subaerially erupted rocks along the length of the East African Rift. These mantle sources are: the depleted upper mantle, the Afar mantle plume, and the Pan-African lithosphere which is defined by as the mixing of three mantle source end-members (Rooney et al., 2012; Schilling et al., 1992). Measuring the volatile contents of the same Gulf of Aden glasses measured for their Sr-Nd-Hf-Pb isotopic compositions will provide direct and quantitative constraints on the volatile contents of each of these three mantle sources. These volatile contents can be used to benchmark the nature of the geophysical anomaly in each region and together will present hypotheses about the possible volatile contents of the solid sources in between volcanic centers along the rift.

Here, we present major element compositions of naturally glassy, olivine-hosted melt inclusions and their olivine hosts, along with dissolved S and H_2O, and $S^{6+}/\Sigma S$ ratios in the glassy melt inclusions from Erta Ale volcano (Figure 4). This data will be combined with previously collected datasets from the same volcano (Field et al., 2012; de Moor et al., 2013), and used to assess the relative importance of various differentiation processes prior to and during eruption of the host tephra, and to constrain pre-erupted water concentrations of magmas at Erta Ale volcano. We also present new S and H_2O measurements of the same submarine glasses, as well as $S^{6+}/\Sigma S$ and $Fe^{3+}/\Sigma Fe$ ratios from

the Gulf of Aden (Figure 5) that were previously measured for major, trace, and radiogenic isotope compositions (Schilling et al., 1992). These measurements will be used to determine the volatile contents of each of the three major mantle sources that contribute to the magmas of the Gulf of Aden, Afar Triangle, and the Main Ethiopian Rift. From this, we assess the importance for the range of the observed slowness of seismic waves in the region.

Geological setting

Erta Ale

Erta Ale volcano is a basaltic shield volcano that lies at the northern terminus of the subaerial portion of the East African Rift, in Ethiopia (Figure 4). This volcano has two pit craters, one in the northern and one in the central region of the caldera, and an elliptical, 0.9 by 1.9 km, "summit sink" that is elongated in the NW-SE direction (Zelenski et al., 2013). For many decades, Erta Ale has sustained a continuously convecting lava lake (Spampinato et al., 2008). This lava lake was first observed in 1967 (Barberi & Varet, 1970); however, it is thought to have existed earlier than this due to previous reports of a smoking mountain and glowing red summit observed by visitors. In November of 2006, the lava lake displayed crusted areas delineated by hot cracks, and continuous resurfacing (Spampinato et al., 2008). The last eruption occurred in November of 2010 with an estimated total volume erupted of ~0.006 km^3 (Field et al., 2012) of plagioclase + clinopyroxene + olivine-bearing basalt. The lava flow filled the central pit crater, and overflowed into the main crater constructing a small cinder/spatter cone around the lava lake crater (de Moor et al., 2013). Recent lava flows within the summit sink are composed of plagioclase porphyritic basalts; however, the base of the volcano is olivine basalt. These lavas display a similar composition to older erupted rocks (Barberi & Varet, 1970; Field et al., 2012).

Gulf of Aden

The Gulf of Aden is located east of the Afar triangle (Figure 5) and is a young ocean basin with well-defined continental margins and an active mid-ocean ridge spreading center (called the Sheba Ridge) that is defined by fracture zones and a rift valley (Cochran, 1981). East of 45°E, the Gulf of Aden has been actively spreading for approximately 10 m.y, whereas west of 45°E is thought to have separated in the last 3-4 m.y due to westward rift propagation into the Afar (Schilling et al., 1992). There are no definitive ages available for lavas west of 48°E (Bosworth et al., 2005), however the majority of this region is composed of fresh basaltic pillow lavas with pristine glassy rinds that are presumably younger than ~1 Ma (Bosworth et al., 2005; Schilling et al., 1992).

Methods

Sample Descriptions

Erta Ale

The tephra sampled in this study was collected from the cinder/spatter cone of Erta Ale volcano (N13°36.201'; E40°39.800') (Figure 4) formed during the November 2010 overflow and supplied by Tobias Fischer at the University of New Mexico and is the same tephra studied by de Moor et al. (2013). The tephra consists of vesicular, glassy scoria clasts that are < 2 cm in the longest dimension. Olivine, plagioclase, and pyroxene are found throughout the tephra (Figure 3); however, the pyroxene is somewhat less abundant than olivine and plagioclase with ~10% of the tephra consisting of pyroxene, ~40% olivine, and ~50% plagioclase. Olivines (~1-2mm) in this tephra are subhedral to anhedral and are encrusted with matrix glass. These olivines contain several spherical to oblate, pale-brown naturally glassy silicate melt inclusions that are ~150-250 μm in diameter. The pyroxenes (~1-2mm) are deep green in color, are subhedral to anhedral and are encrusted in matrix glass. About one to two naturally glassy spherical to oblate silicate melt inclusions are found towards the center of the pyroxenes that are ~90-250 μm in diameter. The plagioclase (~1-2mm) are milky white in color, and anhedral. These plagioclase grains contain several spherical to oblate pale brown naturally glassy silicate melt inclusions that are ~60-300 μm in diameter.

Gulf of Aden

The samples in this study were dredged in 1976 during R/V Vema cruise 33-07, where sampling of the ridge axis took place using physiographic, structural, and magnetic anomaly maps (Schilling et al., 1992). Most of the basalts collected in the Gulf of Aden were from fresh pillow and sheet flow types, with fresh glass present on many of the basalts (Schilling et al., 1992). The samples provided consist of naturally glassy, pale brown, submarine glass chips (~2-4mm) that is very brittle and contain some cracks. Some samples contain small olivine and plagioclase phenocrysts (~60-100 μm), that are anhedral to subhedral.

Sample Preparation

The samples were soaked in deionized water for 24 hours to remove any water soluble sulfate and then dried at 120°C, lightly crushed, and sieved to < 2 mm and > 0.25 mm (de Moor et al., 2013). After being rinsed in deionized water again, the samples were dried, and progressively sorted by size using 10, 20, and 200 mesh metal sieves. Olivine and pyroxenes of around 1-2 mm in size were picked and placed into mineral oil. Upon cleaning off the mineral oil, the samples were mounted in epoxy and single polished until target melt inclusions were exposed at the surface for electron microprobe analysis.

Electron probe micro-analysis

Olivine-, plagioclase-, and pyroxene-hosted melt inclusions from Erta Ale and matrix glasses adhered to the outside of these mineral grains, and submarine pillow glasses from the Gulf of Aden were exposed on a single side and polished for electron probe micro-analysis (EPMA) using a JEOL-JXA 8200 Superprobe at the University of California Los Angeles for major element analyses of glass inclusions and phenocryst hosts. During major element analysis the beam was operated at 15 nA, an accelerating voltage of 15 keV and a focused beam. Sodium and potassium were measured first to minimize alkali loss, with 10 s peak count times. Following this, Si, Ti, Al, Fe*, Mn, Ca, and P were measured with 10-120 s peak count times, with both Ni and Fe* at 120 s. All data were subject to ZAF correction procedures. Primary calibration standards include VG-A99 glass, anorthite, Ti albite, K feldspar, sphene, manganese, and durango apatite. The VG-A99 glass was monitored as secondary standards during each run. Sulfur and chlorine were measured separately using a beam operated at 80 nA, an accelerating voltage of 15 kV and 10 μm beam diameter. Barite and Ba-Cl apatite were used as the primary calibration standard. The VG-A99 glass was monitored as secondary standards during each run.

During analysis of S and Cl compositions of the olivine, plagioclase, and pyroxene melt inclusions, the beam was operated at 80 nA and a 10 μm beam diameter at an accelerating voltage of 15 kV. Pyrite, barite, Ba-Cl apatite, and BAAP syn were used as primary standards and VG-A99 was ran as a secondary standard. The major element compositions of the olivine, plagioclase, and pyroxene hosts were measured adjacent to

the glass inclusions. A focused electron beam was operated at 15 nA and an accelerating voltage of 15 kV. Forsterite, Ni olivine, and magnetite were used as primary calibration standards. VG-A99 and San Carlos olivine were used as secondary standards during each run. Significant olivine zoning was not observed for any samples in this study.

FTIR analysis

After EPMA of melt inclusions, all sample pits were polished away, being careful to account for possible beam damage within the activation volume of each EPMA spot. Melt inclusions were then polished from the opposite side until doubly exposed, and samples were wafered to a thickness of 17 μm-78 μm to create wafers with analyzable pools of optically clear glass. All wafered samples were washed gently with acetone to remove epoxy residues. Dissolved H_2O and CO_2 concentrations in glass inclusions were analyzed by Fourier-transform infrared (FTIR) spectroscopy at the University of California, Riverside. All samples were analyzed using a Thermo Scientific Nicolet iS50 Foruier-transform infrared spectrometer with a Nicolet Continuum Fourier-transform infrared microscope attachment. Spectra for all samples were collected between 1000 and 6000 cm^{-1} using a tungsten-halogen source, KBr beamsplitter and a liquid nitrogen cooled MCT-A detector. The bench, microscope, and samples were continuously purged by air free of water and carbon dioxide using a Whatman purge-gas generator. Aperture dimensions were selected for each sample depending on the geometry of free glass pathway, ranging in size from 11 μm x 14 μm to as large as 100 μm x 145 μm. The thicknesses of each sample were measured using a piezometric digimatic indicator.

XANES analysis

The $S^{6+}/\Sigma S$ ratios of melt inclusions were determined by micro-X-ray absorption near-edge structure (μ-XANES) spectroscopy at beamline 13-IDE, Advanced Photon Source, Argonne National Laboratory. Spectra were collected in fluorescence mode from 2447 eV to 2547 eV, with a dwell time of two seconds on each point, using a Si [111] monochromator and a defocused beam, with effective diameter of ~20 μm. Counts were recorded on a multi-element silicon drift detector X-ray spectrometer, equipped with two Si drift diode detectors. All analyses were done in a helium atmosphere to avoid interaction between the incident photon beam and atmosphere. Incident beam intensity was attenuated using several layers of aluminum foil yielding a photon dosage on the order of $\sim 10^9$ photons per second per μm^2, reflecting a balance between the intensity required to produce interpretable S-XANES spectra from materials with low S-abundances (i.e., < 1000 ppm) and the mounting evidence that very high photon density fluxes electronically damage Fe and S in silicate materials (e.g., Brounce et al., 2017; Cottrell et al., 2018). Each analysis was performed using a stationary beam. Spectral merging, background subtraction, and normalization for these spectra was done using the X-ray absorption spectroscopy data software package ATHENA (Ravel and Newville, 2005), applied uniformly to all spectra so that the region from 2447-2462 eV varies around a value of 0 and region from 2485-2457 varies about a value of 1. These normalized spectra were then subject to spectral fitting routines using the Peak ANalysis (PAN) software package. Each normalized spectrum was fit between 2462-2487 eV with

four Gaussian curves – one for the background (peak center fixed at 2485 eV) and one each for sulfate (peak center fixed at 2481 eV), the broad sulfide feature (peak center fixed at 2477 eV), and the narrow sulfide feature (peak center fixed at 2470 eV). The integrated $S^{6+}/\Sigma S$ ratios reported in Table 1 and 2 were calculated using the area under the curve of the 2485 eV peak divided by the area under the curve of the 2477 eV peak.

$Fe^{3+}/\Sigma Fe$ ratios of submarine pillow glasses from the Gulf of Aden were determined by μ-XANES spectroscopy at beamline 13-IDE, Advanced Photon Source, Argonne National Laboratory. Spectra were collected in fluorescence mode from 7020 eV to 7280 eV using a Si [111] monochromator and a defocused beam diameter of ~50 μm. Counts were recorded on a multi-element silicon drift detector x-ray spectrometer, equipped with two Si drift diode detectors. Eight layers of aluminum foil were placed in the path of the incident photon beam to decrease the intensity of the photon beam prior to interaction with the sample surface, which could lead to auto-oxidation of Fe species dissolved in the glass. The incident photon beam intensity resulted in on the order of $\sim 10^9$ photons per second per μm^2. The Fe-XANES spectra were normalized, and the pre-edge features were fit following the techniques of Brounce et al. (2017), using two background functions and two Gaussian curves to fit the Fe^{2+} and Fe^{3+} peaks. The calibration glasses of Cottrell et al, (2009) and Zhang et al., (2018) were used to calculate $Fe^{3+}/\Sigma Fe$ ratios from the ratio of the areas of the two Gaussian features fit to the pre-edge peaks.

Results

Major and volatile element compositions of Erta Ale melt inclusions and Gulf of Aden glasses

Erta Ale melt inclusions

Erta Ale melt inclusions are trapped in olivines that range in composition from Fo_{79} to Fo_{80}, plagioclase that range in composition from An_{71} to An_{82}, and pyroxene that range in composition from Di_{89} to Di_{92}. The major element compositions of these inclusions were assessed for the effects of post-entrapment crystallization of the host mineral on the edges of the melt inclusions as follows. For olivine grains, we assumed $Fe^{2+}/Mg\ K_D^{ol/liq} = 0.3$ (Roeder & Emslie, 1970). We added olivine with a composition in equilibrium with the melt inclusion back to the melt in 0.1% increments until the melt inclusion reached a composition in equilibrium with the host olivine. The amount of olivine added back to the melt inclusions by this correction ranged from 0 to 0.8% and the corrected melt inclusion compositions contain 6.3-6.5 wt% MgO (Table 1). For pyroxene grains, the Diopside-Hedenbergite component of a modeled pyroxene that is in equilibrium with the measured melt inclusion composition was calculated according to the model of Putirka (1999). This predicted equilibrium composition was then compared to the measured composition of the pyroxene host. Any melt inclusion-host pair that was >4 units apart was disregarded from further consideration and do not appear in the figures that follow (Figure 6). For plagioclase grains, the anorthite component of a modeled plagioclase that is in equilibrium with the measured melt inclusion composition was

calculated using the Post-Entrapment Crystallization MELTS calculator of Kress & Ghiorso (2004). This predicted equilibrium composition was then compared to the measured composition of the plagioclase host. Any melt inclusion-host pair that was > 4 units apart was disregarded from further consideration and do not appear in the figures that follow (Figure 6). In this way, we limit the effects of post-entrapment crystallization in our data consideration.

After assessing for the effects of post-entrapment crystallization, the major element compositions of the accepted inclusions are basaltic, and range in composition from 4.9-6.8 wt% MgO, 10.5-12.9 wt% FeO*, 9.0-11.3 wt% CaO, 0.6-0.9 wt% K_2O, and 2.1-2.7 wt% TiO_2 (Figure 7; Table 1). The K_2O, FeO*, and TiO_2 contents of Erta Ale inclusions are negatively correlated with MgO (i.e., increase with decreasing MgO contents; Figure 7A-C), while CaO is positively correlated with MgO (Figure 7D). Matrix glass adhered to the outside of olivine, plagioclase, and pyroxene grains that contain the melt inclusions measured here was also analyzed, and these matrix glass compositions range from 6.2-6.5 wt% MgO, 11.0-11.3 wt% FeO*, 10.9-11.1 wt% CaO, 0.59-0.66 wt% K_2O, and 2.4-2.5 wt% TiO_2 (Figure 7; Table 1). There is no distinction in major element compositions of melt inclusions according to the identity of the mineral host (plagioclase, pyroxene, and olivine).

Erta Ale melt inclusions range from 0.05 to 0.4 wt% H_2O and 30 to 1220 ppm S. The FTIR spectral measurements of melt inclusions from this study displayed no detectable CO_2 for any melt inclusions. The S contents of Erta Ale inclusions range widely from 30 ppm to 1220 ppm S, but are uncorrelated with FeO* (i.e., FeO*

concentrations range narrowly between 11 and 12 wt% FeO* while S concentrations change by ~25x) (Figure 8A). Sulfur contents are also uncorrelated with H_2O, though H_2O varies from ~0.05-0.4 wt% H_2O (Figure 8C). The H_2O contents of Erta Ale inclusions are uncorrelated with MgO (Figure 8D) and importantly, K_2O. The H_2O concentrations preserved in these inclusions vary by ~a factor of 7, while K_2O concentrations vary by ~a factor of 1.5 (Figure 8B). Olivine hosted melt inclusions extend to higher sulfur concentrations (~1218 ppm) than plagioclase or pyroxene hosted inclusions, and pyroxene hosted inclusions have the lowest sulfur concentrations (~136 ppm), overlapping with those of the matrix glass.

Gulf of Aden glasses

Gulf of Aden glasses are basaltic in composition and range in composition from 6.7-11.7 wt% MgO, 8.6-13.4 wt% FeO*, 10.2-12.8 wt% CaO, 0.04-0.7 wt% K_2O, and 0.9-3.4 wt% TiO_2 (Figure 9; Table 2). The FeO* and TiO_2 contents are negatively correlated with MgO (Figure 9A-B), there is no correlation between both CaO and K_2O with MgO (Figure 9C-D). The K_2O contents of Gulf of Aden glasses vary around ~8 wt% MgO from values < 0.1 wt % to as high as 0.7 wt% K_2O, forming three distinct groups. "Low K_2O" glasses contain between 0.0 and 0.2 wt % K_2O (green samples, Figure 9C), "Medium K_2O" glasses contain between 0.2 and 0.5 wt % K_2O (cyan samples; Figure 9C), and a single "High K_2O" glass contains 0.7 wt% (white sample; Figure 9C). The "Low K_2O", "Medium K_2O", and "High K_2O" glasses are each found in specific geographic regions, with some overlapping, in the Gulf of Aden - "Low K_2O" glasses are

mostly found east of 49°E. “Medium K_2O” glasses are found between 43°E and 48°E, and the single “High K_2O” glass is found at 46°E (Figure 5B).

The Gulf of Aden submarine glasses have 0.2-0.8 wt% H_2O and 800-1300 ppm S (Table 2). The FTIR spectra collected on these glasses displayed no detectable CO_2 peaks. The sulfur contents of these glasses are positively correlated with FeO* contents, consistent with S-FeO* behavior of mid-ocean ridge basalts and saturation with a free sulfide phase (Figure 8A; Jenner & O’Neill, 2012). The sulfur contents of these glasses are uncorrelated with H_2O contents (Figure 8C). The H_2O contents of Gulf of Aden glasses are also uncorrelated with MgO (Figure 8D) but are positively correlated with K_2O within each of the “Low K_2O” and “Medium K_2O” groups (Figure 8B). Additionally, the H_2O contents of the “Low K_2O” group are lower than “Medium K_2O”, and the H_2O content of the “High K_2O” glass is the highest.

The oxidation state of sulfur in Erta Ale samples

The S-XANES spectra of Erta Ale melt inclusions exhibit three absorption features. There is a narrow peak at ~2482 eV (Figure 10) ,consistent with the expected energy of S^{6+} absorption (Fleet, 2005). There also two lower intensity absorption features present – one narrow, appearing at ~2468 eV and one broad, appearing at ~2475 eV (Figure 10). Both of these low energy peaks are commonly attributed to the presence of S^{2-} (Fleet, 2005). The calculated $S^{6+}/\Sigma S$ ratios calculated from these spectra range between 0.06 and 0.17, and are uncorrelated with sulfur concentrations, consistent with

similar observations made by de Moor et al., 2013 on melt inclusions from the same sample (Figure 11).

The oxidation state of sulfur and iron in Gulf of Aden samples

The calculated $Fe^{3+}/\Sigma Fe$ values range between 0.15-0.20, and $S^{6+}/\Sigma S$ values range from 0.09-0.27. There are no correlations between either $Fe^{3+}/\Sigma Fe$ or $S^{6+}/\Sigma S$ and any compositional parameter measured here, except that $Fe^{3+}/\Sigma Fe$ ratios are positively correlated with $S^{6+}/\Sigma S$ (Figure 12A) – the sample with the highest $Fe^{3+}/\Sigma Fe$ also has the highest $S^{6+}/\Sigma S$. Both $Fe^{3+}/\Sigma Fe$ and $S^{6+}/\Sigma S$ are uncorrelated with the radial distance from Lake Abhe from which the samples were dredged – in particular, most samples have $Fe^{3+}/\Sigma Fe$ ~0.16 and $S^{6+}/\Sigma S$ ~0.06-0.26 (Figure 12B-C). Additionally, there is no correlation between $S^{6+}/\Sigma S$ and the radial distance of Lake Abhe; however, a "Medium K_2O" sample shows an increase in $S^{6+}/\Sigma S$ (0.27) around 182 km from the lake. The "Low K_2O" samples have the lowest $S^{6+}/\Sigma S$ values (0.09-0.11), and the "High K_2O" sample has $S^{6+}/\Sigma S$ ~ 0.16. Erta Ale samples are similar to that of the "High K_2O" sample, having $S^{6+}/\Sigma S$ values of ~0.16. (Figure 12C).

Discussion

Fe and S redox

We calculated the fO_2 recorded by Erta Ale inclusions relative to the quartz-fayalite-magnetite (QFM) oxygen buffer from their measured $S^{6+}/\Sigma S$ ratios using the calibration of Jugo et al., (2009), yielding a range of fO_2s between $\Delta QFM = + 0.5$ and $\Delta QFM = + 0.7$. This calibration is based off of experiments of hydrous basaltic and andesitic magmas at fixed pressure and temperature and may have limited applicability outside of the experimental exploration, like in the case of the relatively dry Erta Ale melt inclusions studied here. In order to capture the influence of pressure, temperature, water content, and major element compositions on the relationship between S speciation in silicate melts and fO_2, we also calculated fO_2 relative to the QFM buffer by first calculating $Fe^{3+}/\Sigma Fe$ ratios from our measured $S^{6+}/\Sigma S$ ratios according to the modified relationship between Fe-S redox pairs described by Muth & Wallace (2021). The $Fe^{3+}/\Sigma Fe$ ratios of Erta Ale melt inclusions calculated in this way range from 0.15 and 0.16 (in good agreement with previous measurements of melt inclusions from the same eruptive unit at Erta Ale of ~0.16 de Moor et al., 2013). These $Fe^{3+}/\Sigma Fe$ ratios correspond to fO_2s calculated using the calibration of Kress and Carmichael (1991) of $\Delta QFM = 0.06 - 0.25$. There are uncertainties in each approach. On one hand, the calculation of fO_2 from measured $S^{6+}/\Sigma S$ ratios is direct, but we must apply that calibration outside of the bounds of the intended application. On the other hand, the relationship between $S^{6+}/\Sigma S$ and $Fe^{3+}/\Sigma Fe$ ratios in silicate melts at igneous temperatures is actively debated (e.g., Nash et

al., 2019), but the relationship between $Fe^{3+}/\Sigma Fe$ ratios and fO_2 is rigorously defined (e.g., Kress and Carmichael, 1991). A discussion of the relative merits of each approach is beyond the scope of this contribution. We discuss fO_2s determined via the calculation of $Fe^{3+}/\Sigma Fe$ ratios (ΔQFM = 0.16 - 0.25) in what follows.

We calculated the fO_2 from directly measured $Fe^{3+}/\Sigma Fe$ ratios of Gulf of Aden submarine glasses using the calibration of Kress and Carmichael (1991), yielding a range of fO_2s between ΔQFM = 0.15 - 0.32. In addition, as described for the Erta Ale samples above, we also calculated fO_2 recorded by Gulf of Aden submarine glasses relative to QFM oxygen from their measured $S^{6+}/\Sigma S$ ratios using the calibration of Jugo et al. (2009), yielding a range of fO_2s between ΔQFM = + 0.5 and ΔQFM = + 0.8. Finally, we also calculated $Fe^{3+}/\Sigma Fe$ ratios from our measured $S^{6+}/\Sigma S$ ratios according to the modified relationship between Fe-S redox pairs described by Muth & Wallace (2021) as described above for Erta Ale samples. The calculated $Fe^{3+}/\Sigma Fe$ ratios of Gulf of Aden glasses range from 0.15 and 0.17, similar to that of the directly measured $Fe^{3+}/\Sigma Fe$ ratios (0.15-0.20; Table 2).

Crystallization and Degassing

Erta Ale

We modelled the effects of crystallization on residual magma compositions using the Rhyolite-MELTS model of Gualda & Ghiorso (2015) to estimate the effects of fractional crystallization on major element chemistry at a pressure equal to 30 bar, and a starting fO_2 of ΔQFM = 0. At this pressure and starting fO_2, a model melt that begins with

a composition equal to sample BS-h2-MI1(de Moor et al., 2013) crystalizes olivine, clinopyroxene, and plagioclase with small amounts of spinel, apatite, orthopyroxene as it cools from a calculated liquidus temperature of 1168°C to 954°C. As these phases crystallize, the magma composition decreases in MgO content (from a starting value of 6.95 wt% MgO to 0.97 wt% MgO) as TiO_2 and FeO first begin to increase in concentration, then decrease in concentration at ~5 wt% MgO due to the beginning of the crystallization of FeTi oxides. In the same model, K_2O increases continuously as the result of its incompatibility in all the crystallizing phases, and CaO decreases continuously as the result of its compatibility in both plagioclase and pyroxene (Figure 7A-D). This is consistent with the measured compositions of Erta Ale melt inclusions and indicates that the melts trapped by the inclusions studied here underwent 5-41% crystallization from a parental magma similar in composition to sample BS-h2-MI1.

We calculated isobars for a basaltic magma in equilibrium with a C-S-O-H vapor using the D-COMPRESS model of Burgisser et al., (2015). The volatile compositions of Erta Ale melt inclusions are consistent with pressures of entrapment from ~8 to 25 bars (Figure 13), which correspond to depths in the lava lake of ~24-75 m. This is consistent with crystallization of the phenocryst hosts and entrapment of the melt inclusions that we analyzed in those hosts in the lava lake and the shallowest portion of the reservoir beneath it (Moore et al., 2019).

Gulf of Aden

We modelled the effects of crystallization on residual magma compositions using the Rhyolite-MELTS model of Gualda and Ghiorso (2015) to estimate the effects of fractional crystallization on major element chemistry at a pressure equal to 300 bar, and a starting fO_2 of ΔQFM = 0. At this pressure and starting fO_2, a model melt that begins with a composition similar to sample V3307-66D-1g crystallizes olivine, clinopyroxene, and plagioclase as well as small amounts of spinel and apatite as it cools from a calculated liquidus temperature of 1278 °C to 900 °C. As these phases crystallize, the magma composition decreases in MgO content (from a starting value of 11 wt% MgO to 0.08 wt% MgO as TiO_2 and FeO first increase slightly in concentration, then increase more rapidly at around 9 wt% MgO due to the crystallization of plagioclase and their incompatibilities in those phases, then begin to decrease at around MgO ~ 4.8 wt% due to the start of crystallization of FeTi oxides from the magma (Figure 9A-B), while K_2O increases as the result of its the incompatibility in all crystallizing phases (Figure 9C). In the same model, CaO first begins to increase in concentration due to its incompatibility in olivine, which is the only crystallizing phase between 12 and 9 wt% MgO, then begins to decrease slightly between 7 and 9 wt% MgO due to the crystallization of plagioclase, then decreases more rapidly due to the crystallization of pyroxene (Figure 9D). This model is broadly consistent with the measured compositions of Gulf of Aden glasses and indicates that the melts trapped by the glass studied here underwent 1-51% crystallization from a parental magma similar in composition to sample V3307-66D-1g.

We calculated the pressure of H_2O saturation of Gulf of Aden glasses using the VolatileCalc model of Newman & Lowenstern (2002). These glasses reflect volatile saturation pressures of between 3 and 66 bars, which would correspond to depths in the water column of ~9-198 mbsl. These samples were dredged from the seafloor between 800 and 3492 mbsl (corresponding to a pressure of the water column at the time of eruption of ~81-354 bar), indicating that volcanic degassing of S and H_2O has not affected the measured volatile contents of these samples.

Regional variations in volatiles and redox

Submarine pillows (including the same samples studied here) from the Gulf of Aden and various lavas from the Main Ethiopian Rift have been measured for Sr-Pb-Hf-Nd isotopic compositions to assess the role of multiple mantle and lithospheric components in melt generation along the East African Rift (Rooney et al., 2012; Schilling et al., 1992). These studies reveal variations in the Sr-Pb-Nd-Hf isotopic compositions in lavas erupted along the rift. Furthest to the east and in the realm of "normal oceanic spreading" environment, the East Sheba Ridge lavas (East of ~52°) have $^{206}Pb/^{204}Pb$ (18.3-18.5), $^{87}Sr/^{86}Sr$ (0.702), ε_{Hf} (12.8-18.4), and ε_{Nd} (8.2-9.9) that define the expected values of each isotope ratio in the depleted upper mantle that feeds the mid-ocean ridge spreading system (14A-D). This isotopic endmember is defined by global mid-ocean ridge basalts, and is referred to as the Depleted MORB Mantle, or DMM.

Moving west along the Gulf of Aden spreading centers towards the East African margin, the West Sheba Ridge lavas (between 44°E and 51°E) vary more widely in each

isotope ratio, including extending to higher $^{206}Pb/^{204}Pb$ (18.2-19.4) and $^{87}Sr/^{86}Sr$ (0.702-0.703), and lower ε_{Hf} (8.3-20.4), and ε_{Nd} (4.6-10.3) compositions (14A-D). Importantly, the highest $^{206}Pb/^{204}Pb$ and $^{87}Sr/^{86}Sr$ and lowest ε_{Hf} and ε_{Nd} values are found in the same samples: V3307-50D-1g and geographically adjacent samples, and these samples have been used as the defining presence and maximum influence of the Afar mantle plume in the mantle sources of these lavas (Schilling et al., 1992). From these isotopic studies, the Afar mantle plume has been characterized as a so-called "FOZO" or "C, or Common" or "PREMA" plume (Schilling et al., 1992; Rooney et al., 2012), whose radiogenic isotopic compositions are dominated by contributions of some component in the mantle that all mantle plumes sample to some degree (hence the moniker Common, or PREMA – PREvalent MAntle). The physical nature of this component is not well understood, but it has been suggested that it may be in or sample directly the transition zone or lowermost mantle.

The Asal/Tadjoura samples (42°E and 44°E) display some variation in $^{206}Pb/^{204}Pb$ (18.5-18.8), $^{87}Sr/^{86}Sr$ (0.703-0.704), ε_{Hf} (10.5-16.2) and ε_{Nd} (4.9-6.8) that define the expected values of each isotope ratio of the Pan-African lithosphere (Schilling et al., 1992) (Figure 14A-D). To the south and on the African continent, the Main Ethiopian Rift samples show a wide variation of $^{206}Pb/^{204}Pb$ (18.1-18.9), $^{87}Sr/^{86}Sr$ (0.703-0.704), ε_{Hf} (2.4-10.7) and ε_{Nd} (2.3-4.9) and little variation in distance from -238 to -495 km (note values are negative because the sample locations lie on the SW and NW side of Lake Abhe whereas the others lie to the east) (Figure 14A-D).

In the east, in the realm of normal ocean spreading, East Sheba Ridge samples have measured H_2O contents (this study) of 0.15-0.37 (Figure 15B) and $Fe^{3+}/\Sigma Fe$ ~0.16 (Figure 12B). This is overlapping with H_2O and $Fe^{3+}/\Sigma Fe$ constraints of global mid ocean ridge basalts and together with their radiogenic isotopic compositions, indicate that the mantle sources of East Sheba Ridge pillow lavas are equivalent to that of DMM sampled by mid ocean ridge basalts globally. Moving west along the Gulf of Aden spreading centers, H_2O contents of the samples with the highest $^{206}Pb/^{204}Pb$ and $^{87}Sr/^{86}Sr$ and lowest ε_{Hf} and ε_{Nd} are ~0.84 wt% H_2O (Figure 15B) and $Fe^{3+}/\Sigma Fe$ of ~0.16 (Figure 12B). This indicates that the Afar plume may have somewhat elevated H_2O contents, but not substantially different $Fe^{3+}/\Sigma Fe$ from DMM. This is consistent with constraints on $Fe^{3+}/\Sigma Fe$ ratios of glasses (Brounce et al., 2022) and V in olivines (Nicklas et al., 2022) from Reunion Island – another "FOZO" type mantle plumes – that suggests FOZO-type mantle sources are not more oxidized than MORB mantle sources (i.e., DMM). Continuing west, and including subaerially erupted lavas at Erta Ale, samples have measure measured H_2O contents 0.05 to 0.4 wt% (Figure 15B) and $Fe^{3+}/\Sigma Fe$ of ~0.16 (Figure 12B). This indicates that the Pan-African lithosphere may have somewhat elevated H_2O contents, but $Fe^{3+}/\Sigma Fe$ ratios again that are not substantially different from DMM. We note that our Erta Ale measurements are all degassed to some degree and thus our constraints provide the minimum water content of the Pan-African lithosphere.

Variations in H_2O concentrations could be due to variations in the melting fraction of a mantle source that itself does not vary in H_2O contents – because H_2O is incompatible in mantle minerals olivine, pyroxene, and plagioclase, when a melt is

produced from these minerals, any trace H_2O contained in these minerals will enter the melt. When total melt fraction is low, the concentration of H_2O in that melt is high and when melt fraction increases, H_2O in the melt is diluted and concentration goes down. The same behavior is expected of the similarly incompatible elements K_2O and TiO_2, so we can compare the behavior of H_2O to these major elements to assess the extent to which the observed variations in H_2O contents of erupted glasses along the Gulf of Aden are due to variations in melt fraction, mantle composition, or both. Erta Ale samples have roughly constant and low H_2O/K_2O ratios (~0.3) (Figure 16A). Gulf of Aden samples vary more widely in their H_2O/K_2O ratios – "Low K_2O" glasses have H_2O/K_2O between ~3 and 8 (variations in this ratio are controlled primarily by their very low K_2O values); "Medium K_2O" and "High K_2O" glasses have more constant H_2O/K_2O ratios of ~1 (Figure 16A). Because of their similar incompatibilities, the concentrations of H_2O and K_2O are expected to co-vary during melting and crystallization, and in the absence of any other process will have a constant ratio. If volcanic degassing begins to affect the behavior of H_2O through exsolution from the magma and degassing into a gas phase, H_2O/K_2O ratios will decrease. The variation in H_2O/K_2O ratios in Gulf of Aden samples that are known to not have degassed H_2O is thus substantial and noteworthy and indicates that H_2O contents of the mantle sources of these magmas varies independently from K_2O, i.e., that our observations are not due to variations in melting fraction of the mantle alone.

We can also explore this problem using the K_2O/TiO_2 ratios (Figure 15D). Again, both elements are incompatible in the mantle minerals olivine, and pyroxene, as well as the lower pressure olivine, pyroxene, and plagioclase minerals typical of crystallization

prior to and during eruption. Therefore, if the mantle composition of each element does not change, the ratio of these two elements should be constant. Indeed, K_2O/TiO_2 ratios are low and constant near a value of ~0.06 in the "Low K_2O" Gulf of Aden glasses (Figure 15D). However, K_2O/TiO_2 ratios increase around 49 degrees longitude to a maximum value of ~0.5 in the "High K_2O" Gulf of Aden glass (Figure 15D). These sample glasses have the highest H_2O contents (Figure 15B), and lowest H_2O/K_2O ratios (Figure 16A). When plotted versus the radial distance from Lake Abhe (~273km SE from Erta Ale; e.g., after Rooney et al., 2012), this peak in K_2O/TiO_2 (Figure 15D) ratios and H_2O contents (Figure 15B) occurs at the West Sheba Ridge, in the same samples that have the elevated $^{206}Pb/^{204}Pb$ and $^{87}Sr/^{86}Sr$ isotopic compositions, as well as low ε_{Hf} and ε_{Nd} isotopic compositions that are characteristic of the Afar mantle plume (Figure 14A-D) (Rooney et al., 2012; Schilling et al., 1992). Samples with low K_2O/TiO_2 ratios and H_2O contents (i.e., the "Low K_2O" samples) have low $^{206}Pb/^{204}Pb$ and $^{87}Sr/^{86}Sr$ isotopic compositions, and high ε_{Hf} and ε_{Nd} isotopic compositions that are characteristic of the depleted upper mantle.

Our new volatile and redox measurements show that the Gulf of Aden samples that are isotopically characteristic of the depleted upper mantle have low water contents, near 0.2 wt% H_2O, and $Fe^{3+}/\Sigma Fe$ and $S^{6+}/\Sigma S$ ratios characteristic of MORB, near ~0.15 (Fe) and 0.06-0.11 (S) (from the so-called "Low K_2O" samples). The Gulf of Aden samples associated with the Afar mantle plume have elevated concentrations of H_2O, near 0.84 wt%, and this may result from an association with a trace mineral phase that has high H_2O and high K_2O, but not TiO_2. These plume-influenced samples have

$Fe^{3+}/\Sigma Fe$ and $S^{6+}/\Sigma S$ ratios of ~0.16 (Fe) and 0.17 (S), corresponding to fO_2s of a ΔQFM of 0. These redox measurements indicate that the Afar mantle plume is not substantially different in fO_2 from that of DMM. The Gulf of Aden and Erta Ale samples associated with the Pan-African lithosphere have concentrations of H_2O, near 0.4%, which may be due to degassing considering Nabro and Dabbahu volcanoes, both located in the Afar triangle (Figure 1), point to undegassed H_2O concentrations near 1.3 wt% (Donovan et al., 2018; Field et al., 2012). These samples have $Fe^{3+}/\Sigma Fe$ and $S^{6+}/\Sigma S$ ratios of ~0.16 (Fe) and 0.26 (S), corresponding to fO_2s of ΔQFM = 0. These measurements indicate that the Pan-African lithosphere does not have substantially different fO_2 values from that of both DMM and the plume but does differ in H_2O.

Using the radiogenic isotopic studies of Schilling et al. (1992) and Rooney et al. (2012) as a template and using our new measurements of H_2O and constraints on $Fe^{3+}/\Sigma Fe$ of Gulf of Aden and Erta Ale glasses, we can place quantitative constraints on the H_2O contents and $Fe^{3+}/\Sigma Fe$ ratios of each mantle component – DMM, the Afar mantle plume, and the Pan-African lithosphere. We begin with variations in the values measured directly in the samples, then calculate primary melt compositions (including H_2O and $Fe^{3+}/\Sigma Fe$) to assess the possibility for variations of these values in the mantle sources of these samples themselves.

Primary melt compositions for Low-K, Medium-K, and High-K Gulf of Aden magmas

We estimated primary melt compositions (i.e., compositions immediately before the segregation of primitive melt(s) from their mantle residues, prior to crystallization-

differentiation and degassing) based on our measurements and estimates of the possible range of amounts of crystal fractionation prior to eruption (Table 3). We incrementally added equilibrium liquidus olivine back to the compositions of Low K_2O, Medium K_2O, High K_2O, and Erta Ale samples until they reached equilibrium with Fo_{90} olivine. Calculation of olivine addition was done as described for the post-entrapment crystallization correction for olivine (see Erta Ale melt inclusions section above). This required 1-8.4% olivine addition and produces model melt compositions with 12.0-16.1 wt% MgO, 8.3-11.8 wt% CaO, 0.11 (Low-K) to 0.74 (High-K) wt% H_2O, and $Fe^{3+}/\Sigma Fe$ ratios of 0.13-0.18 (Table 3).

Using the three-component mixing model of Schilling et al. (1992) that is based on the radiogenic isotopic compositions of Gulf of Aden samples, we can calculate the proportion of each component: DMM, the Afar plume, and the Pan-African lithosphere that is required to produce the radiogenic isotopic compositions of Gulf of Aden pillow lavas. We use the same endmember compositions as Rooney et al. (2012), which differ from that of Schilling et al. (1992) in the definition of the isotopic endmember of the Afar plume, which is now thought of as a FOZO plume. We calculate the proportions of DMM to Afar plume to Pan-African lithosphere in High-K glasses, specifically sample V3307-50D-1g, of -6:99:7, in Medium-K glasses of 11-70:25-87:2-4, and in Low-K glasses of 63-88:10-32:2-4. Using $^{206}Pb/^{204}Pb$ and $^{207}Pb/^{204}Pb$ ratios to constrain these proportions, the Low-K samples contain the highest proportion of DMM (63-88%), and the High-K sample can be explained entirely as a melt of the Afar plume (~99%). From this, we

assign the calculated primary H_2O (0.74 wt%) and $Fe^{3+}/\Sigma Fe$ ratio (0.15) from sample V3307-50D-1g as representative of the Afar plume.

We can calculate the fraction of melt required to produce the major element compositions we model here for primary melts after methods described by Kelley et al. (2006), based on primary melt TiO_2 contents (C^1_{Ti}). Using a $D^{mantle/melt}_{Ti} = 0.04$, a mantle source TiO_2 content (C^O_{Ti}) = 0.133 wt%, and the batch melting equation solved for melt fraction:

$$F = \frac{\left(\frac{C^O_{Ti}}{C^1_{Ti}}\right) - D^{mantle/melt}_{Ti}}{\left(1 - D^{\frac{mantle}{melt}}_{Ti}\right)}$$

Our Gulf of Aden primary melts thus reflect melt fractions of their mantle sources of between 0.07-0.1. Using the same batch melting equation, values of F from the TiO_2 solution above, our primary melt H_2O contents (C^1_{H2O}), and $D^{mantle/melt}_{H2O} = 0.012$, we can also calculate the water content of the mantle sources of our Gulf of Aden primary melts, this time solving the batch melting equation for water contents of the mantle source:

$$C^O_{H2O} = C^1_{H2O}\left[F\left(1 - D^{\frac{mantle}{melt}}_{H2O}\right) - D^{mantle/melt}_{H2O}\right]$$

From this calculation, our Gulf of Aden primary melts are produced from solid sources that contain between 0.01-0.06 wt% H_2O. Again, because sample V3307-50D-1g is dominated by contributions from the Afar mantle plume, we assign this mantle source H_2O content (0.06 wt%) to the Afar plume.

Finally, we can combine (1) our calculated mantle source H_2O contents, (2) our constraints on the H_2O content of the Afar plume from sample V3307-50D-1g, (3) the

accepted H_2O content of DMM (from studies of global MORB) equal to 118 ppm H_2O (Kelley et al., 2006), and (4) the fractions of each component (DMM, Afar plume, and Pan-African lithosphere) necessary to describe the Gulf of Aden glasses, to calculate the H_2O content of the Pan-African lithosphere as it is sampled by Gulf of Aden glasses according to:

$$C_{H2O}^{mantle\ source} = C_{H2O}^{DMM} \times m_{DMM} + C_{H2O}^{Afar\ plume} \times m_{Afar\ plume} + C_{H2O}^{Pan\ African\ lithosphere} \times m_{Pan\ African\ lithosphere}$$

Solving for $C_{H2O}^{\text{Pan African lithosphere}}$, we calculate water contents of between 0 and 0.4 wt %, with an average value of 0.17 wt%. This is ~14 times higher than the water content of the depleted upper mantle as sampled by MORB. Partial melts of this hydrous material may mix with magmas produced along the East African Rift and contribute somewhat to the weakening of the African lithosphere and raise the volatile contents of magmas transiting the African lithosphere during rifting.

In table 3 we present a summary of the fractions of melt produced in the mantle under the Gulf of Aden, the H_2O contents of primary melts, the H_2O contents of the mantle sources of each sample for which primary melts were calculated, and the H_2O contents of each endmember component: DMM (Kelley et al., 2006), the Afar plume (this study), and the Pan-African lithosphere (this study). We anticipate that these values will be immediately useful, together with estimates of the potential temperature of the mantle in this region, in quantifying the effect of the presence of melt and H_2O on the nature of the observed geophysical anomaly in the mantle under the East African Rift.

Conclusions

Erta Ale melt inclusions contain 0.05 to 0.4 wt% H_2O and ~0.16 $Fe^{3+}/\Sigma Fe$. They are mostly degassed, reflecting entrapment in the convecting lava lake of Erta Ale. Gulf of Aden submarine glasses contain 0.05 to 0.84 wt% H_2O and ~0.16 $Fe^{3+}/\Sigma Fe$. They constrain the H_2O contents of primary magmas dominated by the depleted upper mantle of 0.14-0.32 wt%, and those dominated by the Afar mantle plume of 0.74 wt%. Following the constraints on volatiles and $Fe^{3+}/\Sigma Fe$ ratios, we used the radiogenic isotopes (Sr-Nd-Hf-Pb) measured by Schilling et al., (1992) to place quantitative constraints on the H_2O contents and $Fe^{3+}/\Sigma Fe$ ratios of each mantle component – DMM, the Afar mantle plume, and the Pan-African lithosphere. From this calculation, because sample V3307-50D-1g is dominated by contributions from the Afar mantle plume, we assign this mantle source H_2O content (0.06 wt%) to the Afar plume, and the Pan-African lithosphere we assign water contents of between 0 and 0.4 wt %, with an average value of 0.17 wt%. We conclude that the Afar mantle plume has H_2O contents elevated above that of DMM, but is not substantially different in redox characteristics. The Pan-African lithosphere is also hydrous relative to DMM and is also not substantially different in redox characteristics. Variations in the proportions of each mantle source along the East African Rift can thus be expected to result in variations in H_2O contents, but not fO_2s, of the parental magmas of the East African Rift. These values combined with estimates of potential temperature, are potentially useful in quantifying the effects of H_2O, or the presence of melt, on the observed geophysical anomaly beneath the East African Rift.

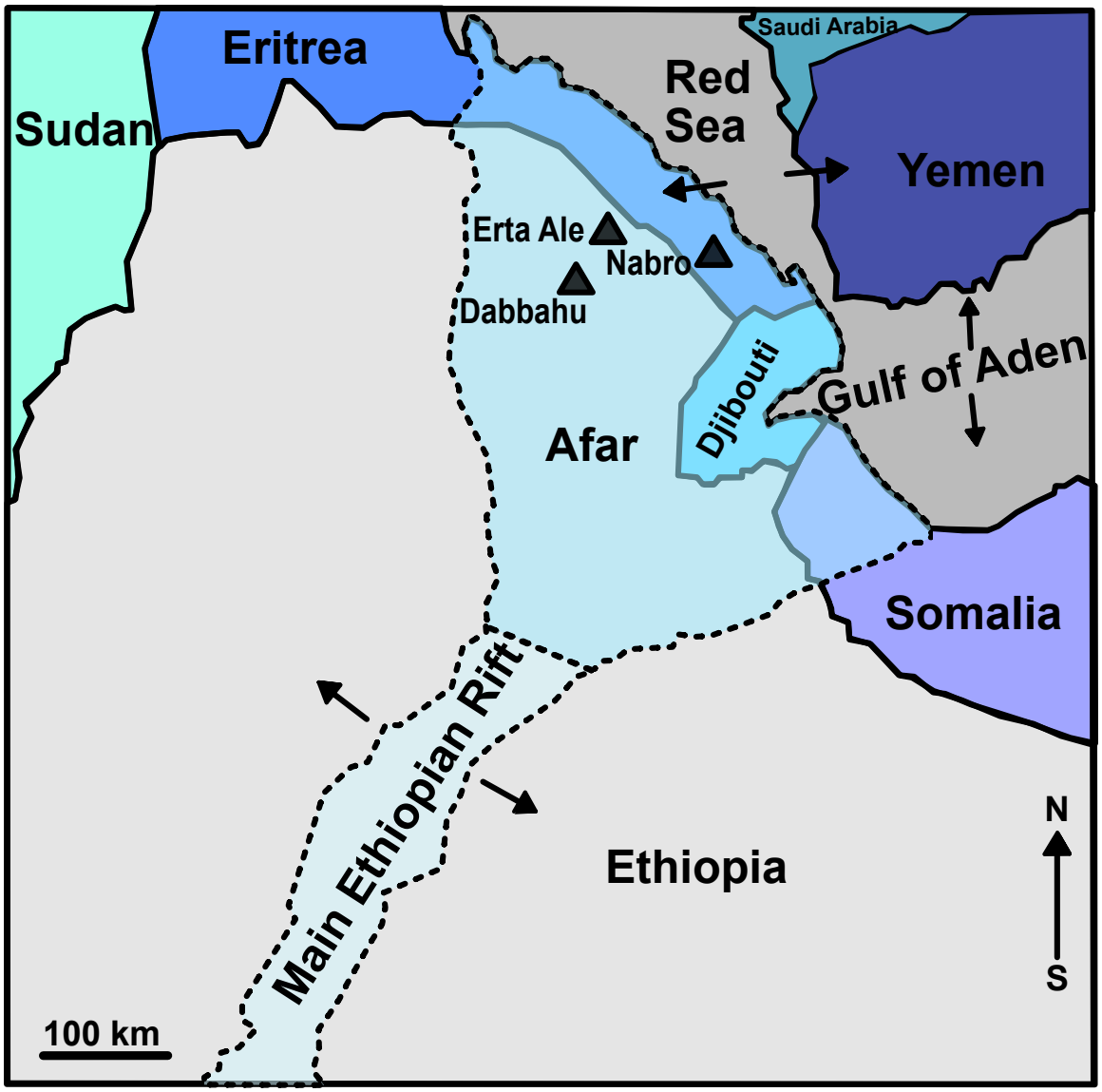

Figure 1. Schematic map showing the relative location of the Main Ethiopian Rift, Afar Triangle, and the Gulf of Aden. The black triangles represent volcanoes as labeled on the map, and the three sets of arrows label the spreading centers and are representative of the Afar Triple Junction. The solid curves represent political boundaries, and the dashed curved represent geological boundaries (e.g., the Afar). Map modified from de Moor et al., (2013) and Field et al., (2012).

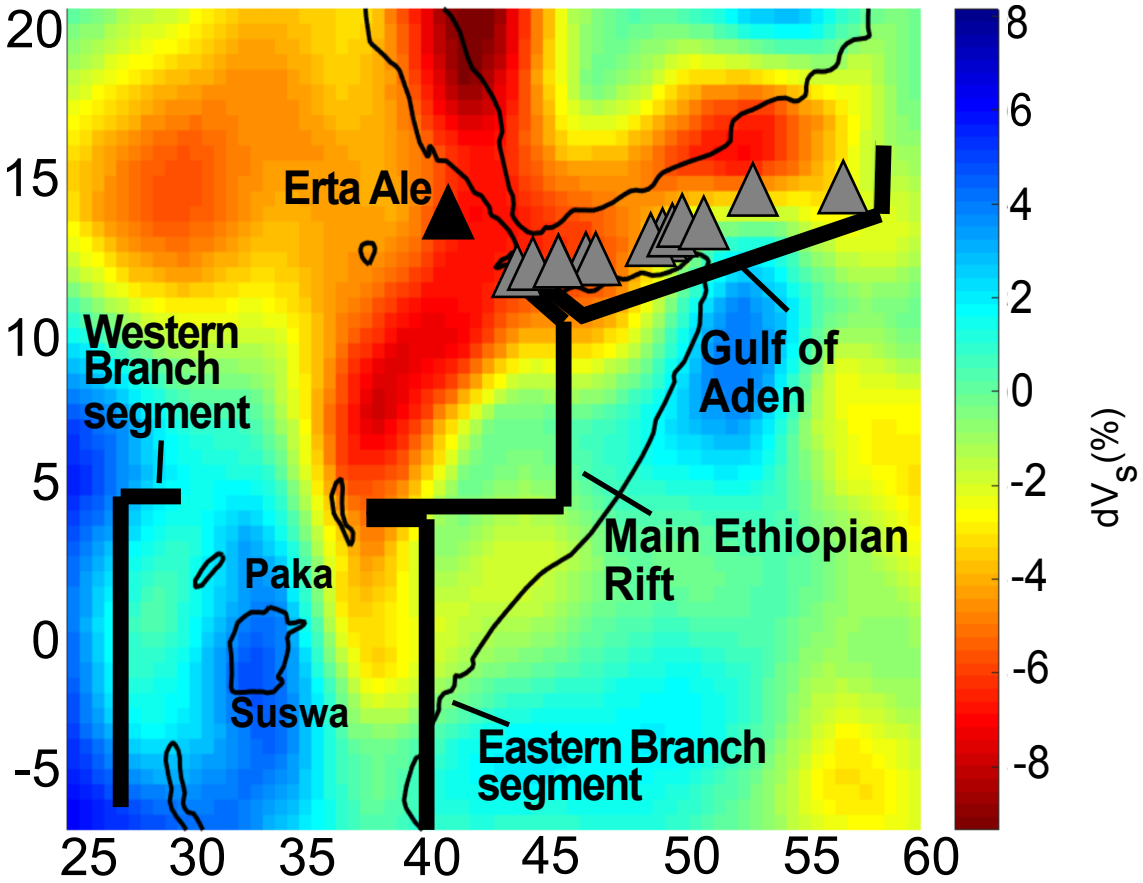

Figure 2. Tomographic plot of the East African Rift region with volcanic samples superimposed. Erta Ale volcano is marked by the black triangle, and the Gulf of Aden sample locations are marked by the gray triangles. The tomographic model shows dVs (%) at 100 km depth (Schaeffer & Lebedev, 2013).

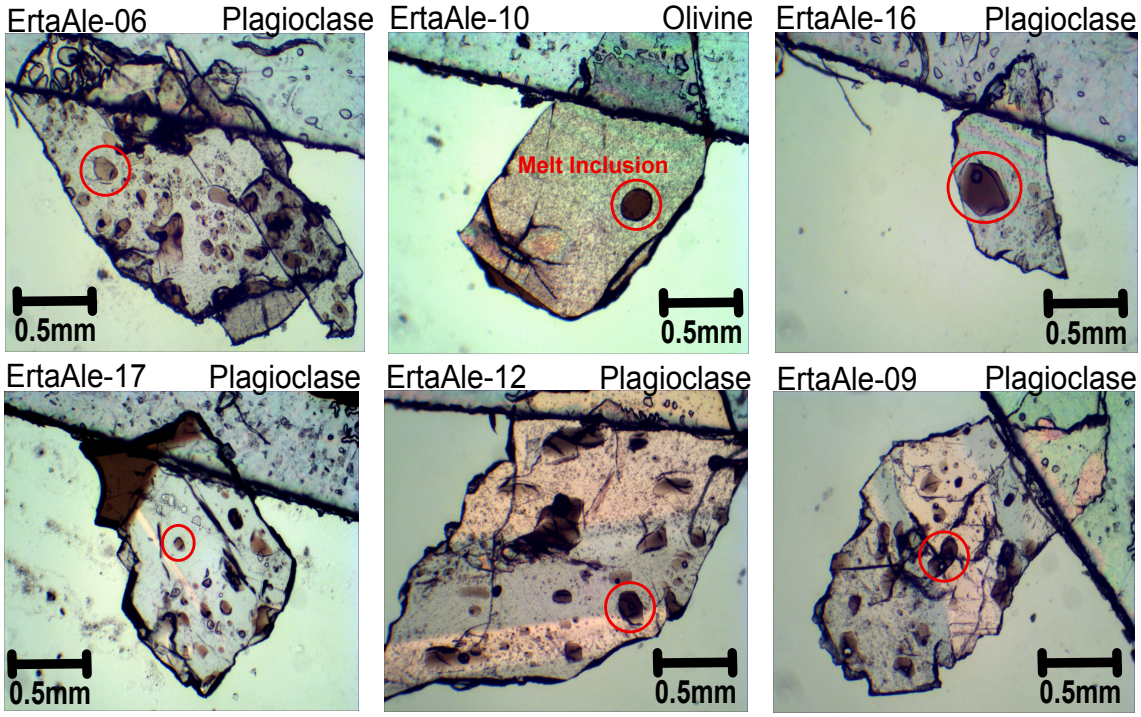

Figure 3. Transmitted light micro photographs of doubly polished olivine- and plagioclase-hosted melt inclusions from this study of Erta Ale.

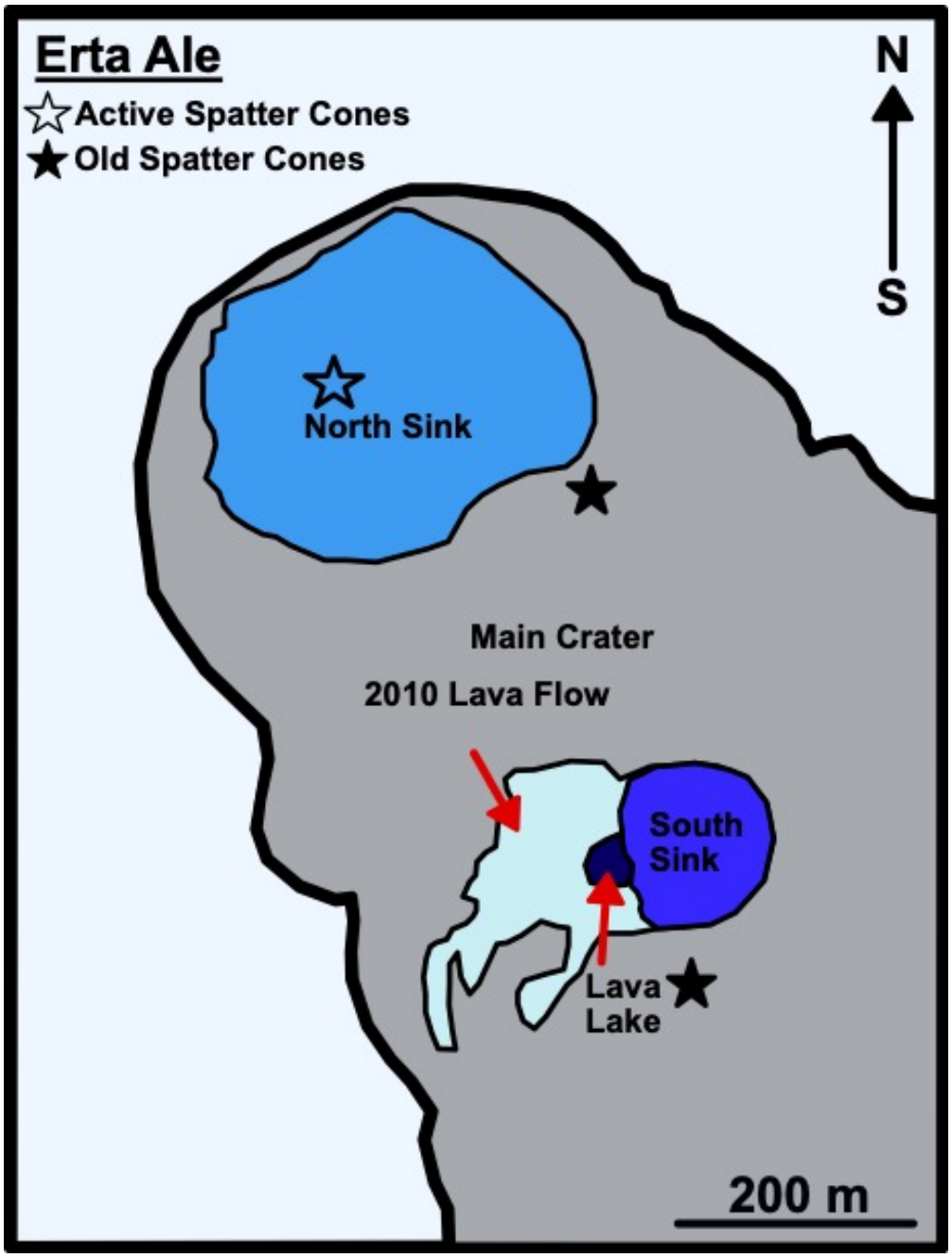

Figure 4. Schematic map of Erta Ale volcano, including the north and south sink craters. Erta Ale samples from this study were collected in the area of the labeled 2010 lava flow. Map modified from Field et al., (2012) and Zelenski et al., (2013).

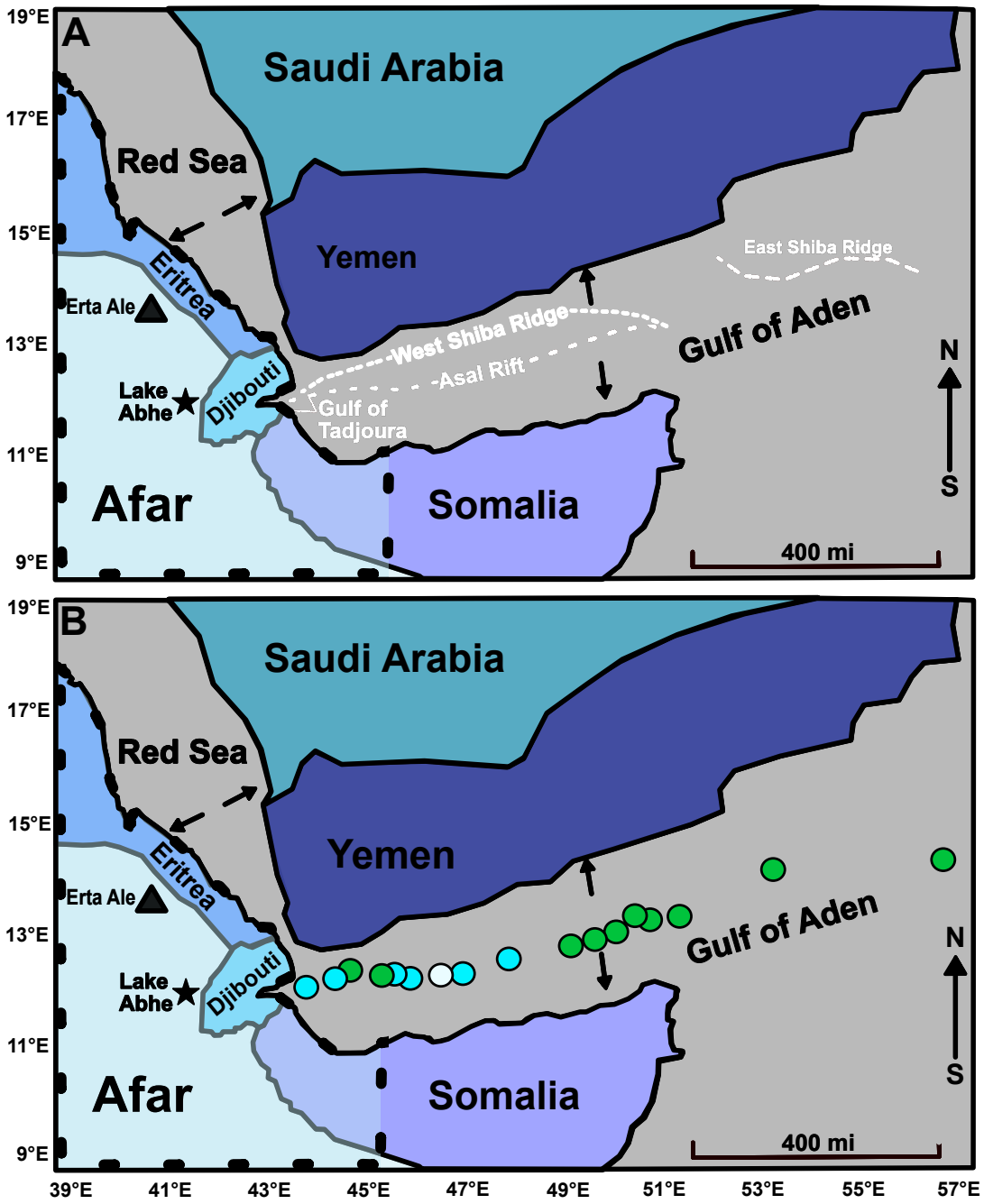

Figure 5. (A) Schematic map of the Gulf of Aden showing the sample locations of Schilling et al., (1992) and this study. Map modified from Rooney et al., (2012). (B) Schematic map of the Gulf of Aden showing the sample locations. The green circles represent the locations of the "Low K_2O" samples, cyan circles represent the "Medium K_2O" samples, and the white sample represents the "High K_2O" sample.

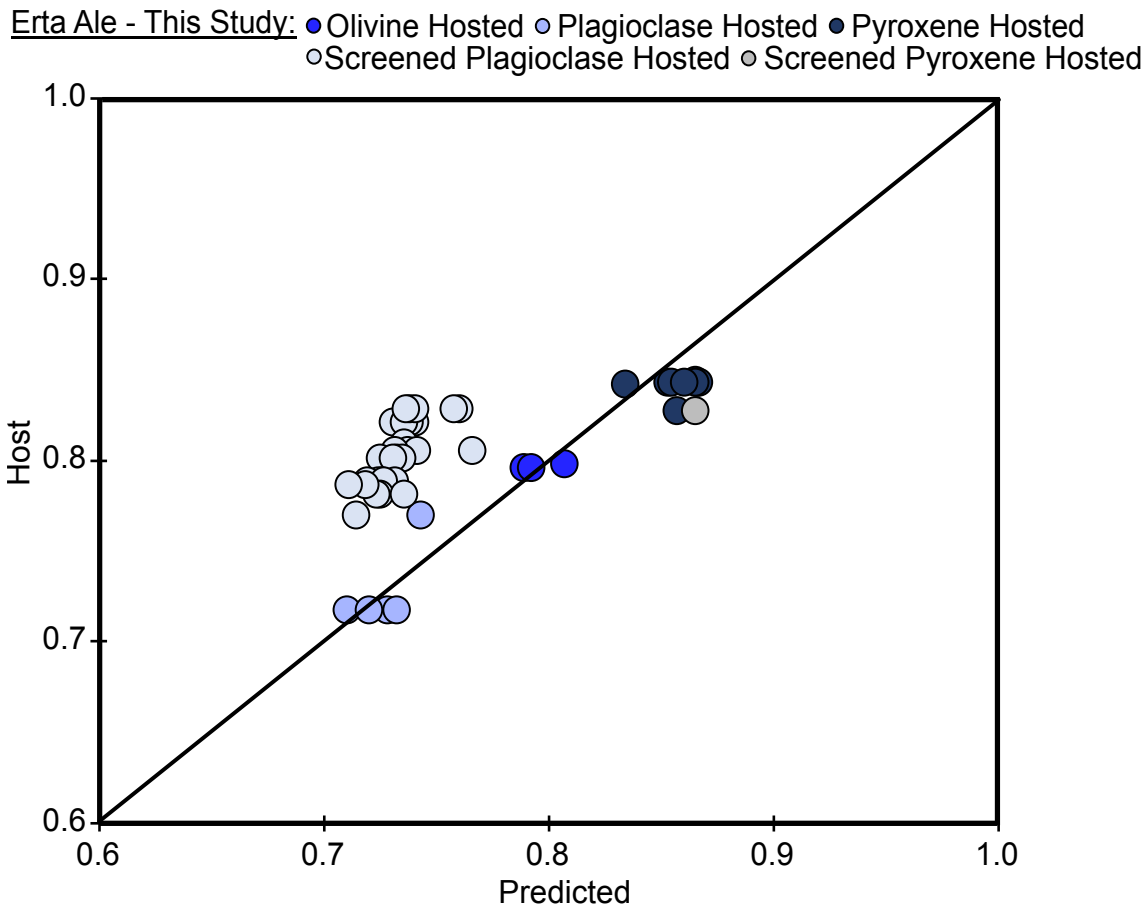

Figure 6. Major element compositions of Erta Ale melt inclusions assessed for post-entrapment crystallization. Samples labeled as "screened" plagioclase- and pyroxene- hosted melt inclusions were disregarded from further consideration.

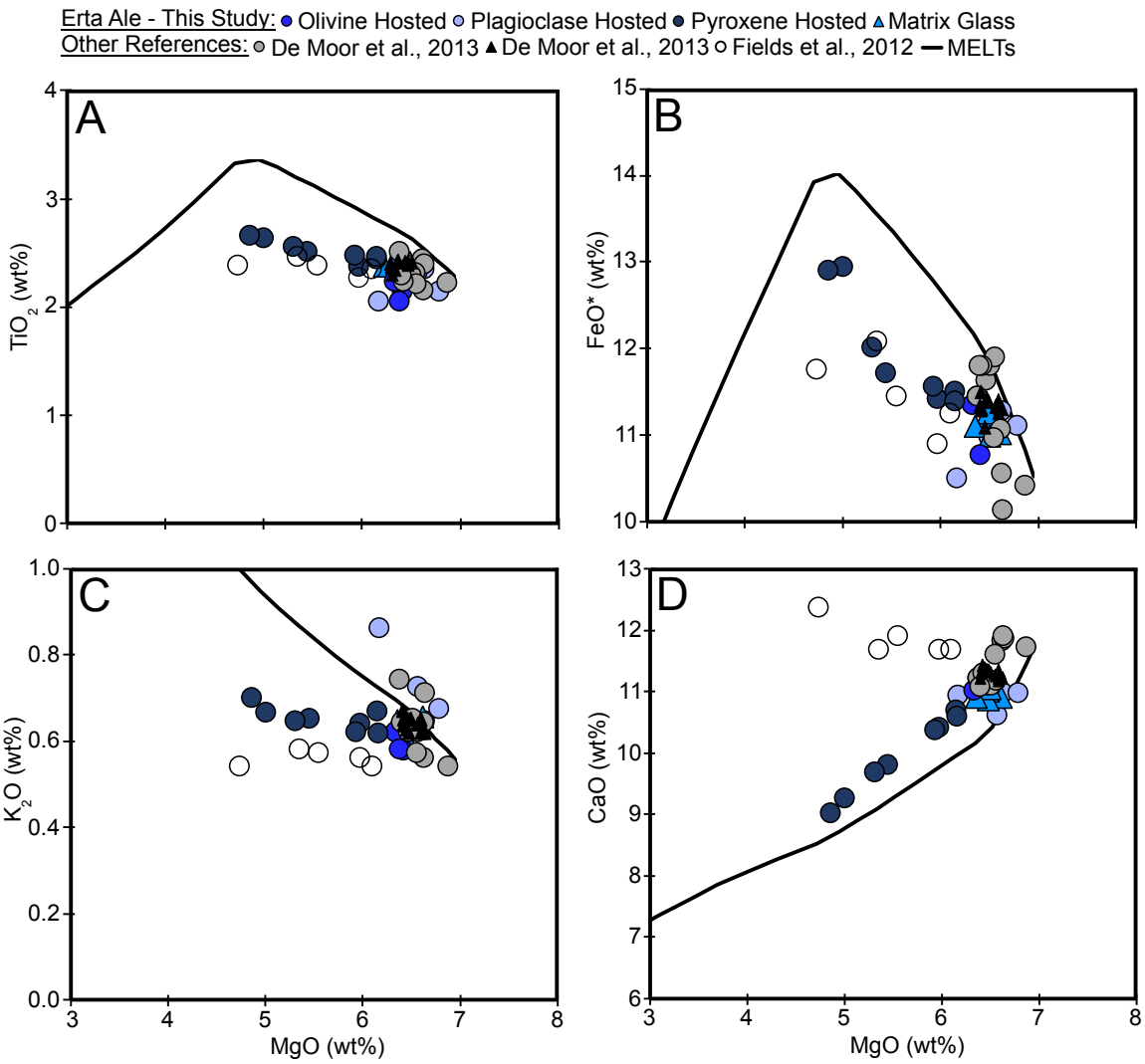

Figure 7. Major element variations for Erta Ale volcano samples. Black curves are MELTs model runs at a pressure of 30 bar, a starting fO_2 of ΔQFM = 0, and a calculated liquidus temperature of 1168 °C to 954 °C. The purple, lavender, and navy Erta Ale samples are melt inclusion data from this study, and the blue circles are matrix glass from this study. Gray circles are olivine- hosted melt inclusions and the black triangles are matrix glass from de Moor et al., (2013) (from the sample samples used in this study). The white circles are olivine-hosted melt inclusions from Field et al., (2012).

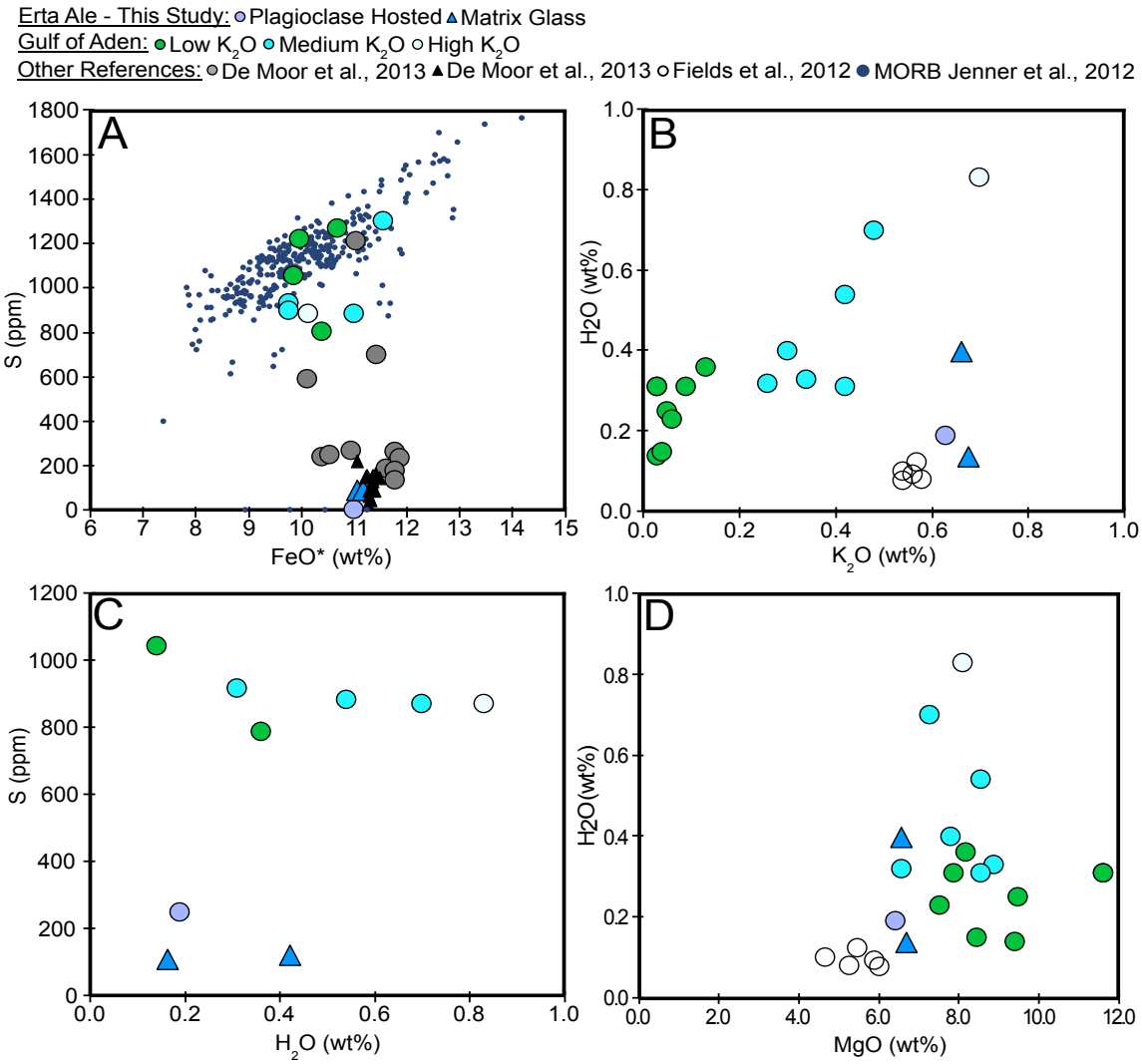

Figure 8. (A) Erta Ale samples display variations in S, and no correlation with Jenner & O'Neill, (2012) MORB data (small blue circles). Gray circles are values from olivine- hosted melt inclusions, and the black triangles are matrix glass from de Moor et al., 2013. Lavender circles are plagioclase- hosted melt inclusions, and the blue triangles are matrix glass from Erta Ale (this study). Gulf of Aden samples, labeled based on the variations of K_2O, The "Low K_2O" (green samples), "Medium K_2O"(cyan samples), and "High K_2O" (white sample) are consistent with Jenner & O'Neill, (2012) MORB data (small blue circles). Samples are submarine glass measurements. (B) Gulf of Aden submarine glass samples (green, cyan, and white) display variation in K_2O and H_2O. Erta Ale samples display variation in H_2O, but little to no variation in K_2O. Field et al., (2012) samples from Erta Ale are from olivine- hosted melt inclusions. (C) Both Erta Ale and Gulf of Aden samples display no correlations between S and H_2O. (D) Both Erta Ale and Gulf of Aden samples display no correlation with MgO.

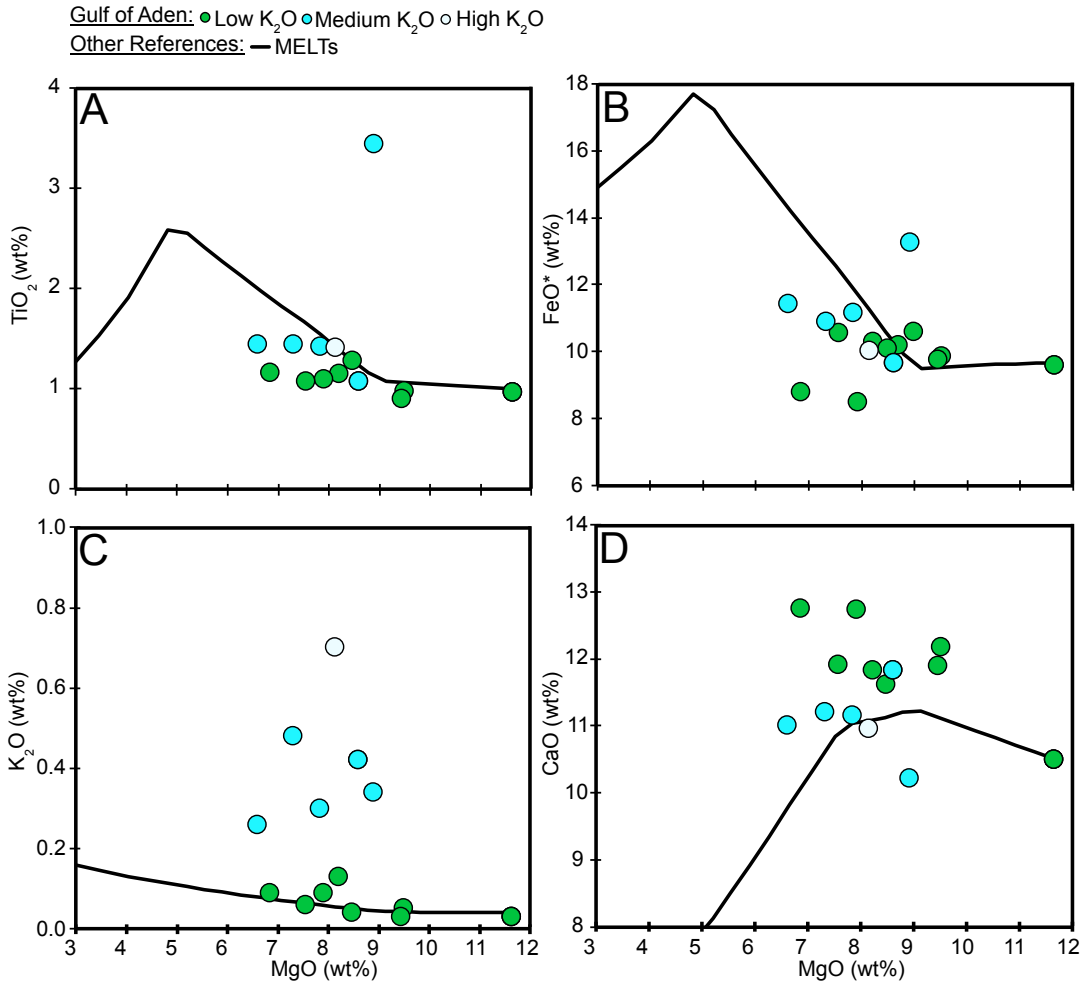

Figure 9. Major element variations for Gulf of Aden submarine glass samples (Kelley et al., 2013). Black curves are MELTs model runs at a pressure of 300 bar, a starting fO_2 of ΔQFM = 0, and a calculated liquidus temperature of 1278 °C to 900 °C. Samples are labeled based on the variations of K_2O. The "Low K_2O" (green samples), "Medium K_2O"(cyan samples), and "High K_2O" (white sample) glasses are each found in specific geographic regions in the Gulf of Aden.

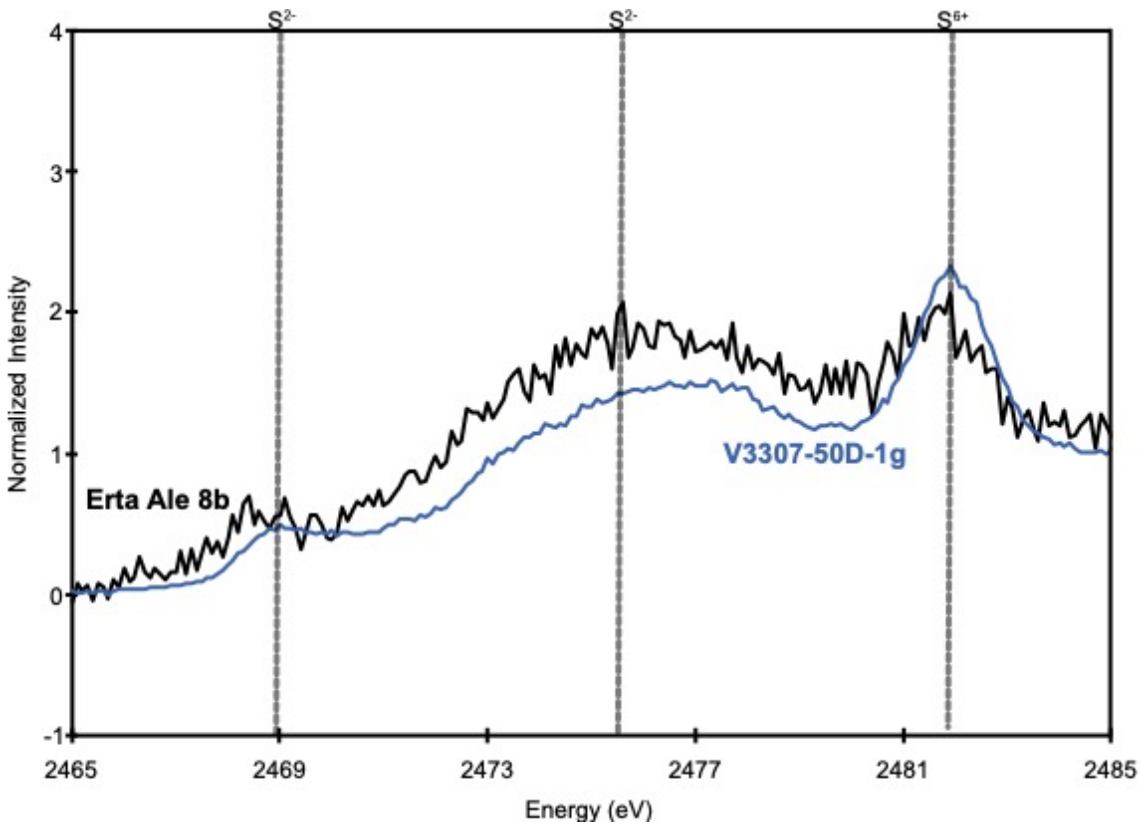

Figure 10. Sulfur XANES spectra for Erta Ale sample 8b displaying a narrow peak at ~2482 eV, one narrow peak at ~2468 eV, and one broad peak at ~2475 eV^{-}. Gray dashed lines show the peak at ~2482 eV is consistent with S^{6+}, and the two peaks at ~2468 eV and ~2475 eV are consistent with S^{2-}.

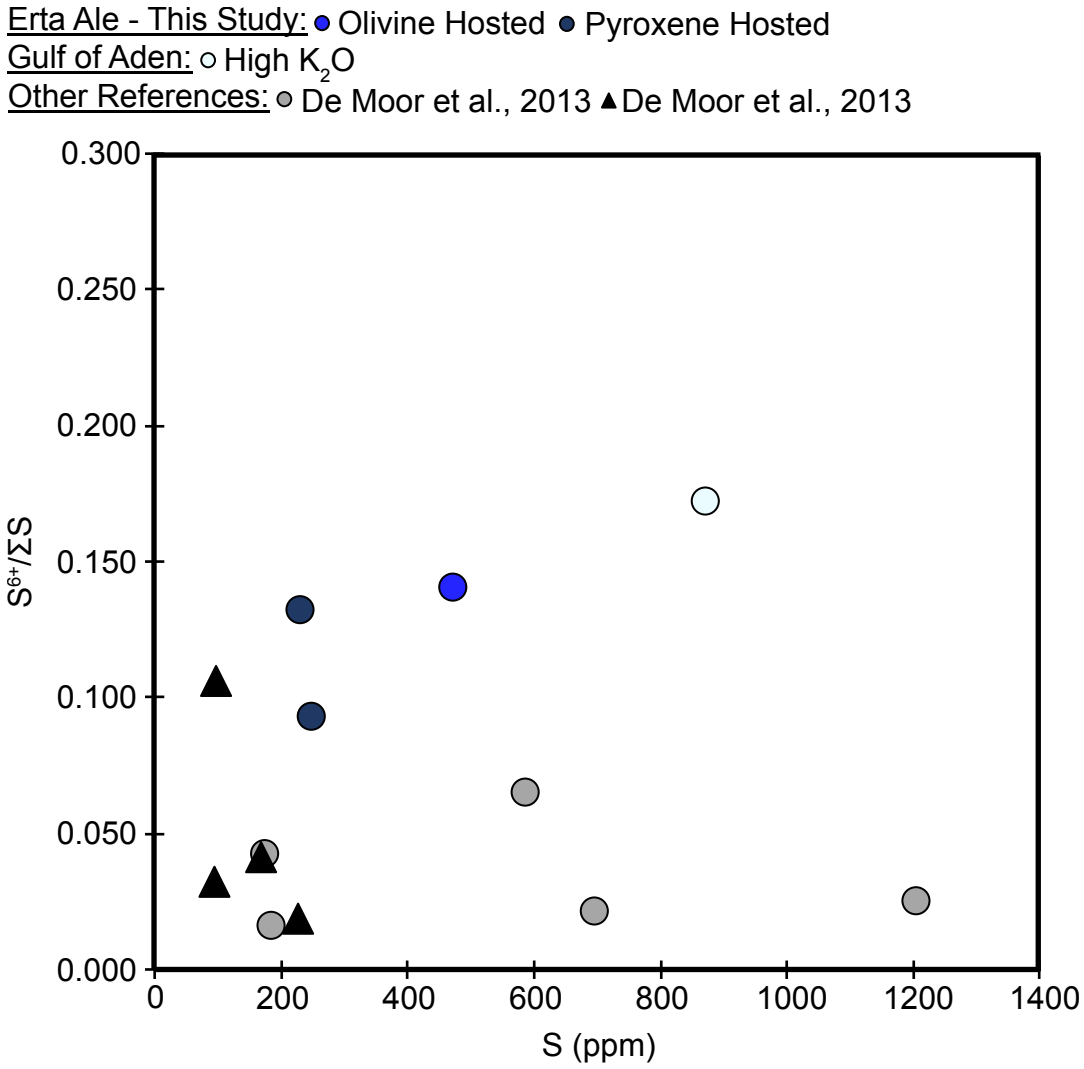

Figure 11. Measured $S^{6+}/\Sigma S$ ratios displaying no correlation with S concentrations, also consistent with observations by de Moor et al., (2013). Erta Ale samples (blue and navy circles) are measured from olivine- hosted melt inclusions, and the "High K_2O" Gulf of Aden sample (white circle) is submarine glass. The gray circles from de Moor et al., (2013) are measured from olivine- hosted melt inclusions, and the black triangles are matrix glass.

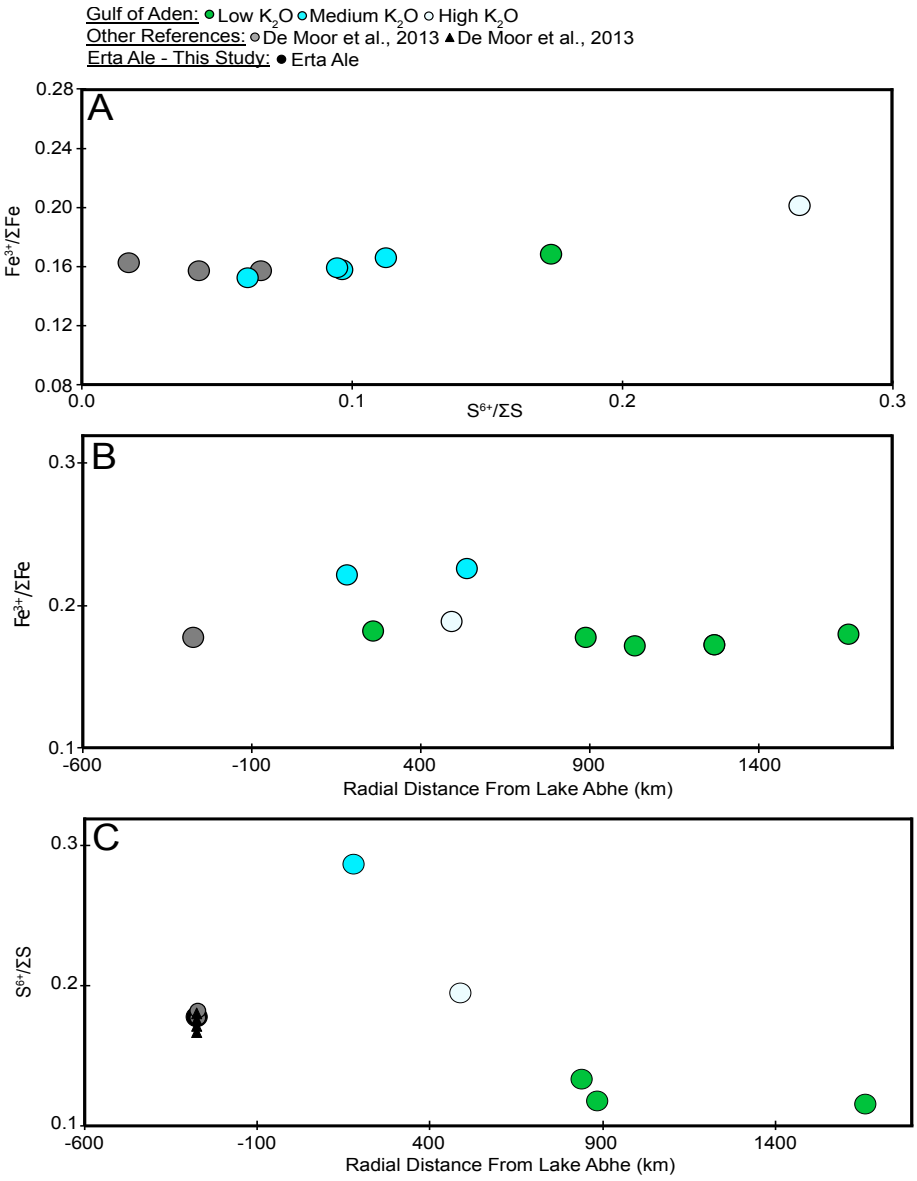

Figure 12. (A) Gulf of Aden and Erta Ale samples display a positive correlation between $Fe^{3+/}\Sigma Fe$ and $S^{6+/}\Sigma S$. Gulf of Aden submarine glass samples are labeled bases on variation of K_2O. The green circles represent the "Low K_2O" samples, cyan circles represent the "Medium K_2O" samples, and the white sample represents the "High K_2O" sample. The gray circles are olivine- hosted melt inclusions from de Moor et al., (2013). (B) $Fe^{3+/}\Sigma Fe$ values for both the Gulf of Aden and Erta Ale display no correlation with the radial distance from Lake Abhe (km). (C) Erta Ale and Gulf of Aden samples display no correlation between $S^{6+/}\Sigma S$ and the radial distance from Lake Abhe (km). The "Low K2O" samples (green) display the lowest $S^{6+/}\Sigma S$ ratios, and a medium K_2O sample (cyan) shows an increase in $S^{6+/}\Sigma S$ ratios around 182km from Lake Abhe. The "High K2O" sample (white) and Erta Ale samples (gray circles, black circles, and black triangles) display similar $S^{6+/}\Sigma S$ ratios of ~0.16.

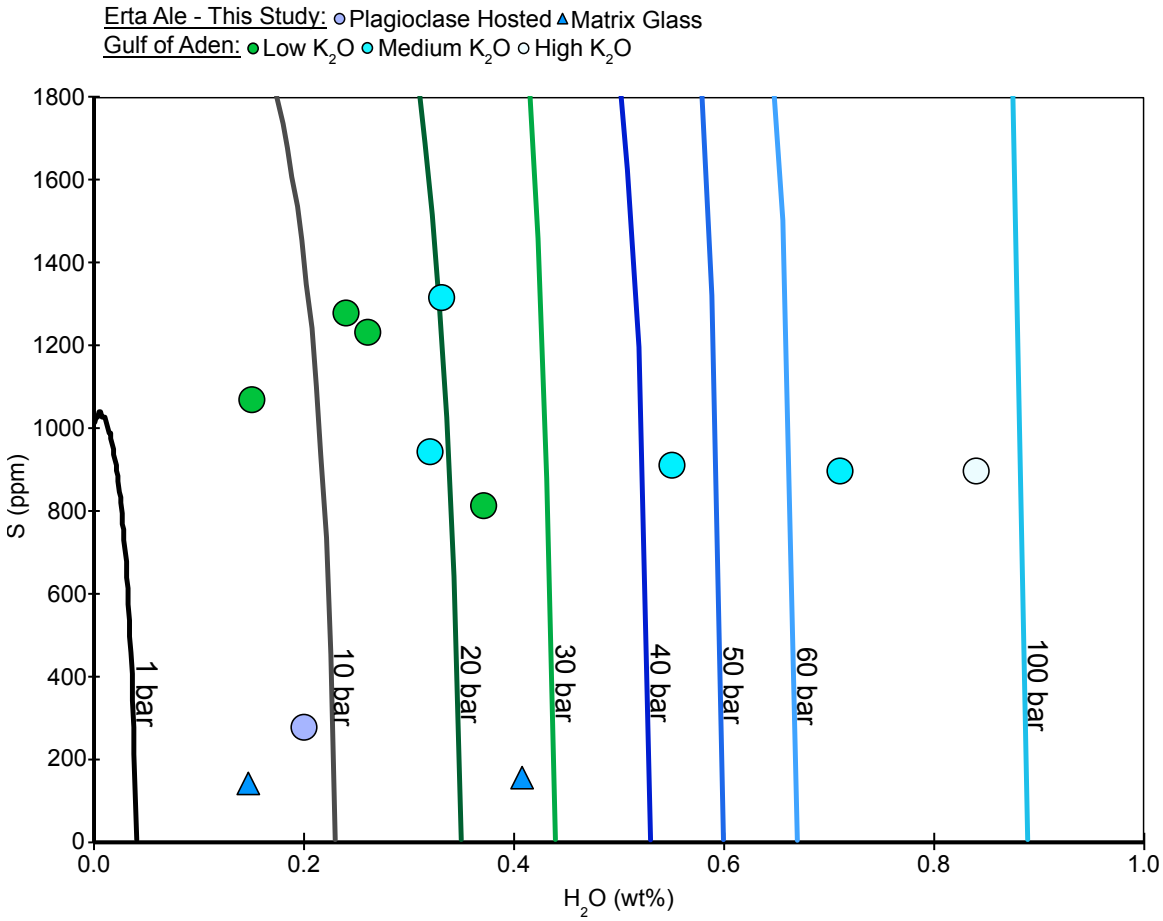

Figure 13. Calculated isobars for a basaltic magma in equilibrium with a C-S-O-H vapor using the D-COMPRESS model of Burgisser et al., (2015). Erta Ale melt inclusions and matrix glass (lavender circle and blue triangles) are consistent with pressures of entrapment from 8 to 25 bars and Gulf of Aden glasses (green, cyan, and white circles) are consistent with volatile saturation pressures of between ~8 and 90 bars.

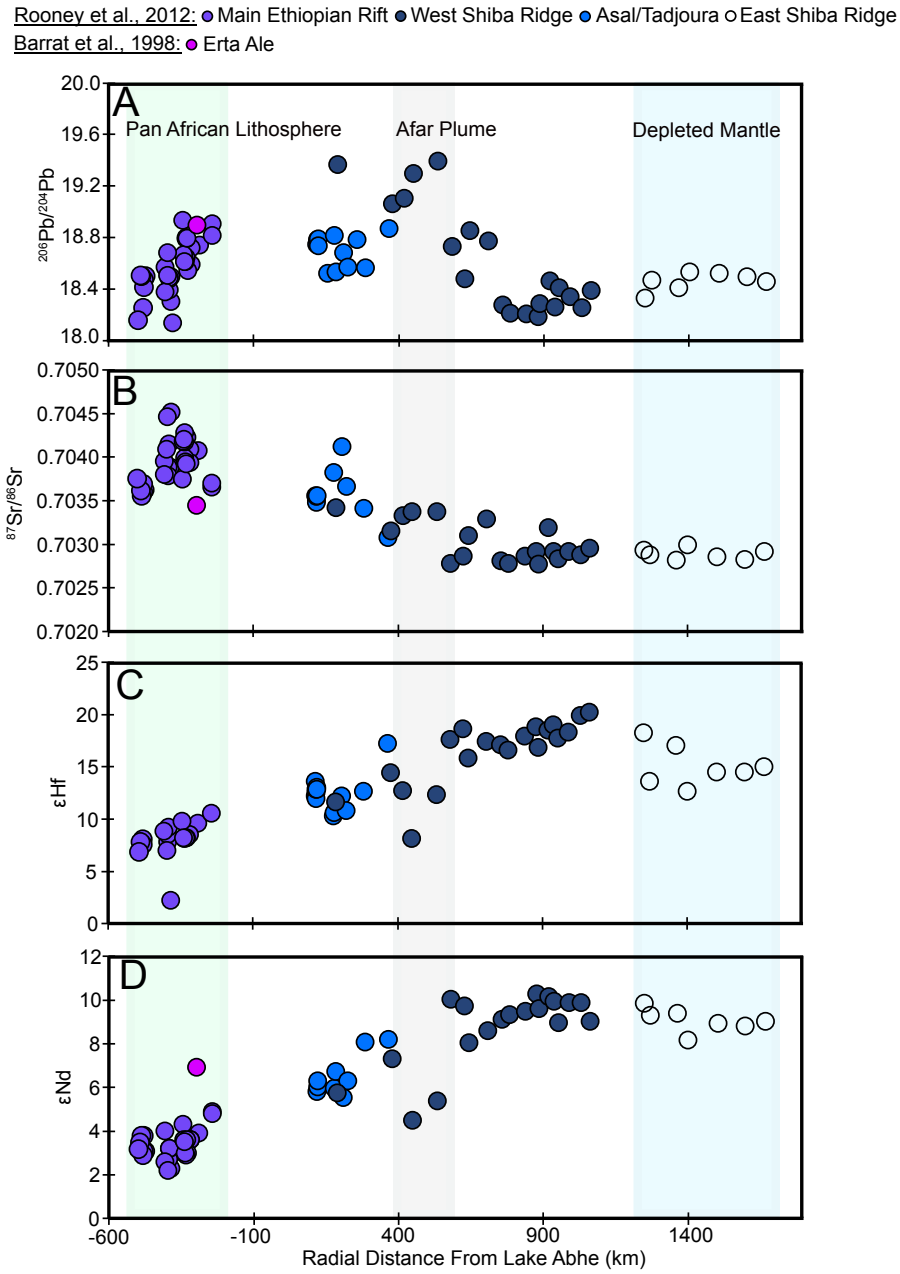

Figure 14. $^{206}Pb/^{204}Pb$, $^{87}Sr/^{86}Sr$, $\varepsilon_{Hf,}$ and ε_{Nd} ratios from the Gulf of Aden and Main Ethiopian Rift. White circles are from the East Shiba Ridge, navy circles are from the West Shiba Ridge, blue circles are from the Asal Rift and the Gulf of Tadjoura, purple circles are from the Main Ethiopian Rift, and the pink circles is from Barrat et al., 1998 Erta Ale samples. The light blue portion of the figure represents the depleted mantle (or "DMM"), the gray represents the Afar Plume, and the green represents the Pan-African lithosphere.

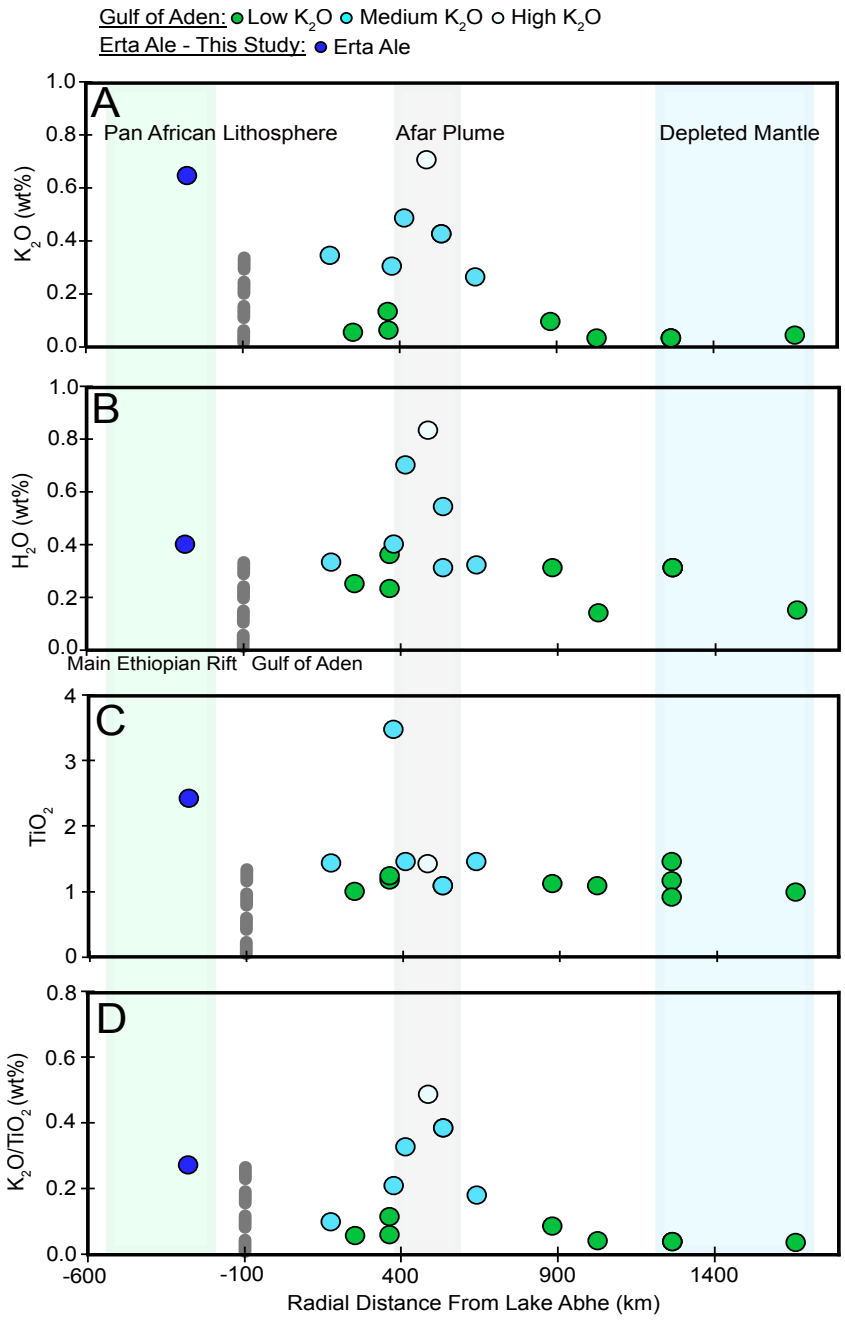

Figure 15. K_2O, H_2O, TiO_2, and K_2O/TiO_2 values from this study versus the radial distance from Lake Abhe. Gulf of Aden glass samples are labeled based on the variations of K_2O. The green circles correspond to the samples that contain Low K_2O contents, cyan corresponds to medium K_2O, and white corresponds to High K_2O. The dark blue circle is from Erta Ale. The light blue portion of the figure represents the depleted mantle (or "DMM"), the gray represents the Afar Plume, and the green represents the Pan-African lithosphere. The short gray dashed line represents the change from the Gulf of Aden to the Main Ethiopian Rift.

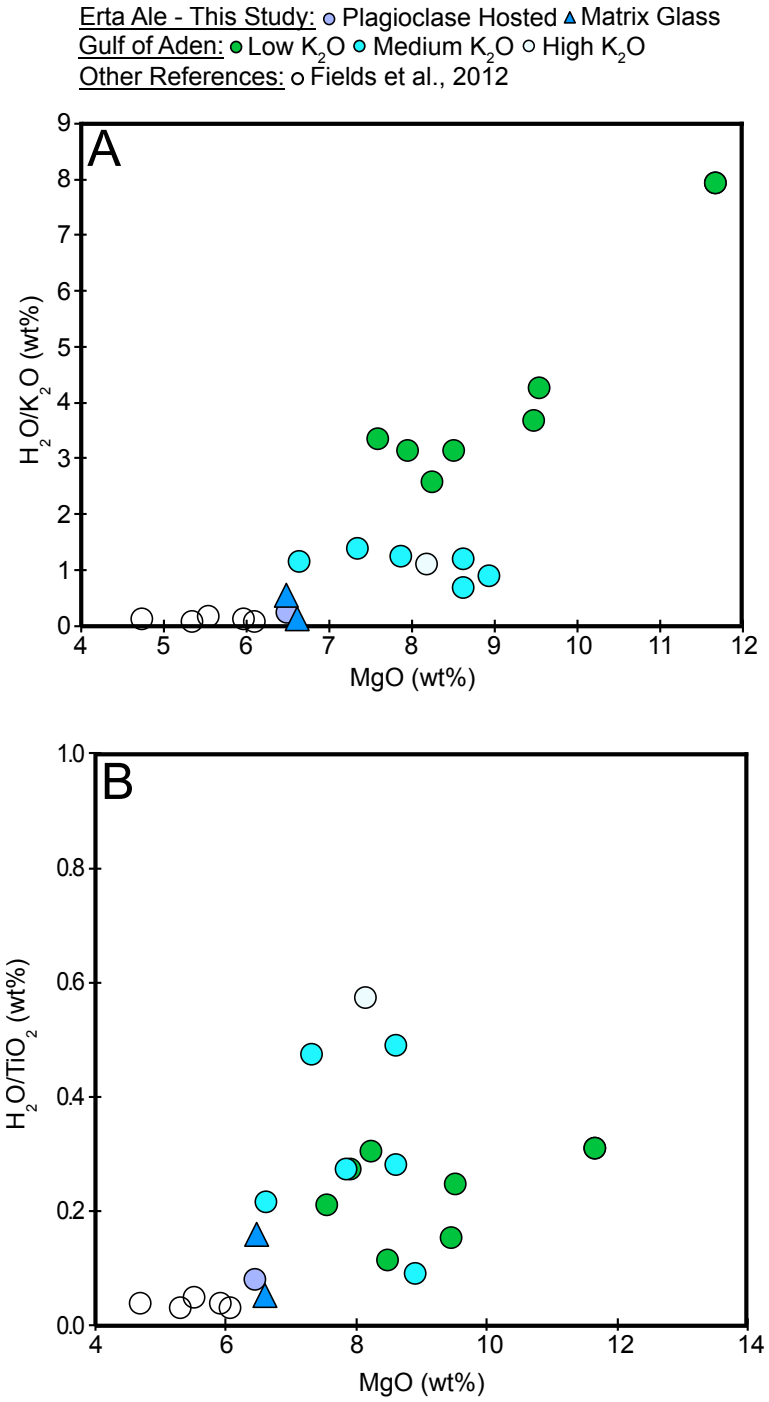

Figure 16. (A) H_2O/K_2O ratios in Erta Ale samples displaying no correlation with MgO. The lavender circle is a plagioclase- hosted melt inclusion, the blue triangles are matrix glass, and the white samples are olivine- hosted melt inclusions from Field et al., 2012. Gulf of Aden glass samples (green, cyan, and white circles) display a positive correlation with MgO. (B) Both Erta Ale and Gulf of Aden samples display no correlation with MgO.

Table 1.
Erta Ale melt inclusion major elements

Sample		ErtaAle-02B	ErtaAle-05A	ErtaAle-05B	ErtaAle-05C	ErtaAle-05D
PEC	(%)	7.70	-	-	2.08	-
T [a]	(°C)	1150	1148	1151	1148	1147
P[b]	(bar)				5	
SiO_2	(wt%)	49.86	49.58	49.72	50.17	49.41
TiO_2	(wt%)	2.08	2.38	2.18	2.29	2.35
Al_2O_3	(wt%)	15.67	13.78	13.80	14.32	13.58
FeO*	(wt%)	10.55	11.32	11.15	11.02	11.12
FeO[c]	(wt%)	8.86	9.62	9.48	9.23	9.45
Fe_2O_3[c]	(wt%)	1.88	1.89	1.86	1.99	1.85
MgO	(wt%)	6.22	6.68	6.83	6.55	6.62
MnO	(wt%)	0.17	0.21	0.19	0.21	0.19
CaO	(wt%)	10.99	11.03	11.03	11.15	10.68
Na_2O	(wt%)	2.65	2.98	3.05	2.99	3.02
K_2O	(wt%)	0.87	0.65	0.68	0.64	0.73
P_2O_5	(wt%)	0.29	0.34	0.27	0.30	0.29
S	(ppm)	520	260	480	260	256
Cl	(ppm)	390	290	290	310	320
H_2O	(wt%)				0.20	
Total	(wt%)	99.69	98.95	98.91	99.27	98.00
$S^{6+}/\Sigma S$						
$Fe^{3+}/\Sigma Fe$[d]						
fO_2[e]						
fO_2[f]						

Table 1 Cont.

Erta Ale melt inclusion major elements

Sample		ErtaAle-12F	ErtaAle-03A	ErtaAle-08A	ErtaAle-08B	ErtaAle-08C
PEC	(%)	-	-	-	-	-
T [a]	(°C)		1135	1134	1139	1125
P[b]	(bar)			17	7	
SiO_2	(wt%)		48.67	49.30	49.58	49.51
TiO_2	(wt%)		2.41	2.51	2.48	2.55
Al_2O_3	(wt%)		14.62	14.45	14.62	15.25
FeO*	(wt%)		11.46	11.61	11.54	11.76
FeO[c]	(wt%)		9.74	9.74	9.63	
Fe_2O_3[c]	(wt%)		1.91	2.08	2.13	
MgO	(wt%)		6.03	5.98	6.20	5.50
MnO	(wt%)		0.21	0.19	0.21	0.20
CaO	(wt%)		10.47	10.43	10.76	9.86
Na_2O	(wt%)		2.89	2.96	2.94	3.16
K_2O	(wt%)		0.65	0.63	0.68	0.66
P_2O_5	(wt%)		0.37	0.35	0.32	0.37
S	(ppm)		136	260	244	260
Cl	(ppm)		280	350	280	270
H_2O	(wt%)	0.15				
Total	(wt%)		97.78	98.41	99.33	98.82
$S^{6+}/\Sigma S$		0.063		0.095	0.134	
$Fe^{3+}/\Sigma Fe$[d]				0.161	0.166	
fO_2[e]				0.18	0.24	
fO_2[f]		0.46		0.56	0.64	

Table 1 Cont.

Erta Ale melt inclusion major elements

Sample		ErtaAle-08D	ErtaAle-08E	ErtaAle-08F	ErtaAle-11A	ErtaAle-13A
PEC	(%)	-	-	-	-	-
T [a]	(°C)	1139	1122	1116	1092	1113
P[b]	(bar)	10	7	8		
SiO_2	(wt%)	49.52	49.57	49.39	44.504	48.77
TiO_2	(wt%)	2.50	2.59	2.67	2.46	2.69
Al_2O_3	(wt%)	14.62	15.28	15.06	15.28	14.85
FeO*	(wt%)	11.43	12.06	12.98	12.67	12.95
FeO[c]	(wt%)				10.68	
Fe_2O_3[c]	(wt%)				2.21	
MgO	(wt%)	6.21	5.36	5.05	3.89	4.91
MnO	(wt%)	0.20	0.20	0.22	0.23	0.23
CaO	(wt%)	10.65	9.74	9.32	7.60	9.07
Na_2O	(wt%)	2.86	3.19	3.18	3.24	3.34
K_2O	(wt%)	0.63	0.65	0.67	0.66	0.71
P_2O_5	(wt%)	0.35	0.38	0.38	0.33	0.36
S	(ppm)	256	220	304	208	184
Cl	(ppm)	270	360	370	340	300
H_2O	(wt%)					
Total	(wt%)	98.96	99.03	98.94		97.87
$S^{6+}/\Sigma S$						
$Fe^{3+}/\Sigma Fe$[d]						
fO_2[e]						
fO_2[f]						

Table 1 Cont.

Erta Ale melt inclusion major elements

Sample		ErtaAle-10A	ErtaAle-14A	ErtaAle-14B	ErtaAle-17matrix
PEC	(%)	-	0.80	0.40	-
T [a]	(°C)	1144	1136	1140	1146
P[b]	(bar)	2	41		3
SiO_2	(wt%)	48.51	49.01	48.52	49.61
TiO_2	(wt%)	2.18	2.27	2.09	2.45
Al_2O_3	(wt%)	14.49	14.20	14.13	14.09
FeO*	(wt%)	10.81	11.39	11.49	11.06
FeO[c]	(wt%)	9.02	9.59	9.66	9.32
Fe_2O_3[c]	(wt%)	2.00	2.00	2.03	1.93
MgO	(wt%)	6.46	6.38	6.43	6.55
MnO	(wt%)	0.17	0.19	0.21	0.21
CaO	(wt%)	11.22	11.08	11.29	10.98
Na_2O	(wt%)	3.04	2.94	2.84	3.06
K_2O	(wt%)	0.59	0.63	0.59	0.66
P_2O_5	(wt%)	0.33	0.37	0.32	0.37
S	(ppm)	484	256	384	124
Cl	(ppm)	230	250	220	210
H_2O	(wt%)				0.15
Total	(wt%)	97.80	98.42	97.90	99.03
$S^{6+}/\Sigma S$		0.142			
$Fe^{3+}/\Sigma Fe$[d]		0.166			
fO_2[e]		0.16			
fO_2[f]		0.66			

Table 1 Cont.

Erta Ale melt inclusion major elements

Sample		ErtaAle-14matrix	ErtaAle-10matrix	ErtaAle-03matrix	ErtaAle-08matrix
PEC	(%)	-	-	-	-
T [a]	(°C)	1143	1143	1143	1140
P[b]	(bar)	17			
SiO_2	(wt%)	48.86	48.48	49.07	49.49
TiO_2	(wt%)	2.44	2.51	2.42	2.42
Al_2O_3	(wt%)	13.92	13.78	13.95	14.37
FeO*	(wt%)	11.23	11.31	11.04	11.16
FeO[c]	(wt%)	9.47	9.54	9.31	9.41
Fe_2O_3[c]	(wt%)	1.96	1.97	1.93	1.95
MgO	(wt%)	6.42	6.42	6.44	6.29
MnO	(wt%)	0.20	0.19	0.21	0.23
CaO	(wt%)	11.08	10.94	11.12	10.99
Na_2O	(wt%)	2.93	3.03	2.85	2.62
K_2O	(wt%)	0.65	0.60	0.64	0.66
P_2O_5	(wt%)	0.37	0.38	0.35	0.33
S	(ppm)	136		92	88
Cl	(ppm)	190		280	270
H_2O	(wt%)	0.41			
Total	(wt%)	98.11	97.64	98.10	98.55
$S^{6+}/\Sigma S$			0.168		
$Fe^{3+}/\Sigma Fe$[d]					
fO_2[e]					
fO_2[f]					

Table 1 Cont.

Erta Ale melt inclusion major elements measured values for PEC compositions reported

Sample		ErtaAle-02B	ErtaAle-05C	ErtaAle-14A	ErtaAle-14B
PEC	(%)	-	-	-	-
T [a]	(°C)	1162	1148	1136	1140
P[b]	(bar)		5	41	
SiO_2	(wt%)	50.11	49.99	49.09	48.56
TiO_2	(wt%)	2.26	2.33	2.29	2.10
Al_2O_3	(wt%)	14.31	13.90	14.31	14.18
FeO*	(wt%)	11.47	11.21	11.33	11.46
FeO[c]	(wt%)	9.67	9.45	9.55	9.66
Fe_2O_3[c]	(wt%)	2.00	1.96	1.98	2.00
MgO	(wt%)	6.76	6.66	6.09	6.29
MnO	(wt%)	0.19	0.21	0.20	0.21
CaO	(wt%)	10.67	11.03	11.17	11.33
Na_2O	(wt%)	2.67	2.98	2.94	2.85
K_2O	(wt%)	0.94	0.66	0.63	0.59
P_2O_5	(wt%)	0.31	0.31	0.37	0.32
S	(ppm)	520	260	256	384
Cl	(ppm)	390	310	250	220
H_2O	(wt%)		0.2	0.67	
Total	(wt%)	99.69	99.27	98.42	97.90
$S^{6+}/\Sigma S$					
$Fe^{3+}/\Sigma Fe$[d]					
fO_2[e]					
fO_2[f]					

Post entrapment crystallization (PEC) corrected values are those with (%) given in the PEC column

*Total Fe content reported as FeO

[a] Temperature calculated from Helz and Thornber (1987)

[b]Pressure calculated using D-COMPRESS of Burgisser et al., (2015)

[c]Calculated value from FeO* and $Fe^{3+}/\Sigma Fe$

[d]Calculated $Fe^{3+}/\Sigma Fe$ after Muth & Wallace., (2021)

[e]fO_2 calculated after Kress and Carmichael., (1991)

[f]fO_2 calculated after Jugo et al., (2009)

Table 2.

Erta Ale phenocryst host major elements

Sample	ErtaAle-02	ErtaAle-03	ErtaAle-05	ErtaAle-12
SiO_2	48.58	50.73	49.89	45.63
TiO_2	0.10	0.76	0.07	0.01
Al_2O_3	32.05	2.47	31.28	32.10
FeO*	0.54	5.80	0.57	0.49
MgO	0.20	16.83	0.22	0.16
MnO	0.03	0.17	0.01	0.00
CaO	15.60	21.04	14.55	16.65
Na_2O	2.55	0.26	3.13	1.87
K_2O	0.11	0.00	0.11	0.05
Total	99.79	98.09	99.83	96.97

Table 2 Cont.

Erta Ale phenocryst host major elements

Sample	ErtaAle-08	ErtaAle-11	ErtaAle-13	ErtaAle-17
SiO_2	51.14	51.40	51.58	48.15
TiO_2	0.74	0.74	0.72	0.07
Al_2O_3	2.43	2.51	2.65	32.83
FeO*	5.63	5.66	5.73	0.49
MgO	16.71	16.47	16.86	0.18
MnO	0.14	0.15	0.17	0.02
CaO	21.05	21.09	20.85	16.23
Na_2O	0.27	0.23	0.25	2.19
K_2O	0.03	0.01	0.01	0.09
Total	98.17	98.25	98.83	100.25

* = total Fe content reported as FeO

Table 3.
Gulf of Aden submarine glass major elements

Sample		V3307-42D-1g	V3307-46D-1g	V3306-39D-1g	V3307-57D-1g
T [a]	(°C)	1207	1181	1197	1153
P[b]	(bar)	7	14		
SiO_2	(wt%)	49.11	50.66	49.99	49.34
TiO_2	(wt%)	1.02	1.19	1.48	1.2
Al_2O_3	(wt%)	15.54	14.83	14.53	17.97
FeO*	(wt%)	9.97	10.4	10.7	8.92
FeO[c]	(wt%)	8.4			7.4
Fe_2O_3[c]	(wt%)	1.8			1.6
MgO	(wt%)	9.6	8.31	9.08	6.94
MnO	(wt%)	0.17	0.18	0.18	0.16
CaO	(wt%)	12.23	11.89	11.17	12.81
Na_2O	(wt%)	2.02	2.1	2.39	2.29
K_2O	(wt%)	0.06	0.14	0.14	0.1
P_2O_5	(wt%)	0.11	0.14	0.18	0.14
S	(ppm)	1216	799		
Cl	(ppm)	155	105		
H_2O	(wt%)	0.26	0.37		
$S^{6+}/\Sigma S$					0.113
$Fe^{3+}/\Sigma Fe$		0.162			0.165
$Fe^{3+}/\Sigma Fe$[d]					0.162
fO_2[e]		0.25			0.24
fO_2[f]					0.60

Table 3 Cont.

Gulf of Aden submarine glass major elements

Sample		V3307-59D-1g	V3307-62D-1g	V3307-61D-2g	V3307-64D-3g
T [a]	(°C)	1175	1191	1168	1206
P[b]	(bar)	11		6	3
SiO_2	(wt%)	49.63	50.03	50.42	49.97
TiO_2	(wt%)	1.14	1.26	1.11	0.94
Al_2O_3	(wt%)	17.03	15.36	15.27	15.4
FeO*	(wt%)	8.6	10.31	10.69	9.87
FeO[c]	(wt%)	7.2			8.4
Fe_2O_3[c]	(wt%)	1.5			1.7
MgO	(wt%)	8.01	8.79	7.65	9.54
MnO	(wt%)	0.16	0.17	0.19	0.17
CaO	(wt%)	12.79	11.42	11.97	11.95
Na_2O	(wt%)	2.3	2.29	2.37	1.95
K_2O	(wt%)	0.1	0.09	0.07	0.04
P_2O_5	(wt%)	0.13	0.15	0.12	0.1
S	(ppm)			1264	1053
Cl	(ppm)			20	85
H_2O	(wt%)	0.32		0.24	0.15
$S^{6+}/\Sigma S$		0.097			
$Fe^{3+}/\Sigma Fe$		0.157			0.151
$Fe^{3+}/\Sigma Fe$[d]		0.158			
fO_2[e]		0.08			0.09
fO_2[f]		0.57			

Table 3 Cont.

Gulf of Aden submarine glass major elements

Sample		V3307-66D-1g	V3307 69D-1g	V3307-47D-1g	V3307-48D-2g
T [a]	(°C)	1250	1186	1173	1163
P[b]	(bar)	11	3	17	46
SiO_2	(wt%)	47.83	50.03	50.59	50.48
TiO_2	(wt%)	1.01	1.32	1.46	1.48
Al_2O_3	(wt%)	16.15	15.31	14.39	14.67
FeO*	(wt%)	9.72	10.23	11.3	11.01
FeO[c]	(wt%)	8.2	8.6		9.1
Fe_2O_3[c]	(wt%)	1.6	1.8		2.1
MgO	(wt%)	11.74	8.57	7.93	7.41
MnO	(wt%)	0.16	0.19	0.19	0.18
CaO	(wt%)	10.55	11.68	11.21	11.26
Na_2O	(wt%)	2.59	2.33	2.29	2.46
K_2O	(wt%)	0.04	0.05	0.31	0.49
P_2O_5	(wt%)	0.1	0.13	0.17	0.33
S	(ppm)				881
Cl	(ppm)				180
H_2O	(wt%)	0.32	0.16	0.41	0.71
$S^{6+}/\Sigma S$		0.062	0.095		
$Fe^{3+}/\Sigma Fe$		0.152	0.159		0.169
$Fe^{3+}/\Sigma Fe$[d]		0.146	0.157		
fO_2[e]		0.15	0.2		
fO_2[f]		0.46	0.56		

Table 3 Cont.

Gulf of Aden submarine glass major elements

Sample		V-60g	V3307-51D-1g	V3307-52D-1g
T [a]	(°C)	1195	1189	1189
P[b]	(bar)	12	30	11
SiO_2	(wt%)		50.69	50.69
TiO_2	(wt%)	3.49	1.11	1.11
Al_2O_3	(wt%)	14.32	14.8	14.8
FeO*	(wt%)	13.4	9.78	9.78
FeO[c]	(wt%)	10.7	7.8	
Fe_2O_3[c]	(wt%)	3.0	2.2	
MgO	(wt%)	9	8.69	8.69
MnO	(wt%)	0.2	0.15	0.15
CaO	(wt%)	10.27	11.89	11.89
Na_2O	(wt%)	2.49	2.09	2.09
K_2O	(wt%)	0.35	0.43	0.43
P_2O_5	(wt%)	0.49	0.19	0.19
S	(ppm)		895	927
Cl	(ppm)		345	415
H_2O	(wt%)	0.34	0.55	0.32
$S^{6+}/\Sigma S$		0.266		
$Fe^{3+}/\Sigma Fe$		0.201	0.205	
$Fe^{3+}/\Sigma Fe$[d]		0.171		
fO_2[e]		0.97		
fO_2[f]		0.83		

Table 3 Cont.

Gulf of Aden submarine glass major elements

Sample		V3307-54D-1g	V3307-50D-1g	V3307-44D-2g
T [a]	(°C)	1149	1180	
P[b]	(bar)	12	66	
SiO_2	(wt%)	50.33	51.11	
TiO_2	(wt%)	1.48	1.45	
Al_2O_3	(wt%)	15.39	14.41	
FeO*	(wt%)	11.56	10.15	
FeO[c]	(wt%)		8.4	
Fe_2O_3[c]	(wt%)		1.9	
MgO	(wt%)	6.7	8.24	
MnO	(wt%)	0.2	0.17	
CaO	(wt%)	11.07	11.02	
Na_2O	(wt%)	2.61	2.32	
K_2O	(wt%)	0.27	0.71	
P_2O_5	(wt%)	0.17	0.26	
S	(ppm)	1300	883	
Cl	(ppm)	190	505	
H_2O	(wt%)	0.33	0.84	
$S^{6+}/\Sigma S$			0.174	0.086
$Fe^{3+}/\Sigma Fe$			0.168	
$Fe^{3+}/\Sigma Fe$[d]			0.166	0.171
fO_2[e]			0.32	
fO_2[f]			0.71	0.54

Major elements by Kelley et al., (2013)

*Total Fe content reported as FeO

[a]Temperature calculated from Helz and Thornber (1987)

[b]Pressure calculated using the VolatileCalc model of Newman & Lowenstern (2002)

[c]Calculated value from FeO* and $Fe^{3+}/\Sigma Fe$

[d]Calculated $Fe^{3+}/\Sigma Fe$ after Muth & Wallace., (2021)

[e]fO_2 calculated after Kress and Carmichael., (1991)

[f]fO_2 calculated after Jugo et al., (2009)

Table 4.

Primary melt major elements and mantle component proportions

Sample		V3307 42D-1g	V3307 59D-1g	V3307 64D-3g	V3307-66D-1g
SiO_2	(wt%)	48.48	48.96	49.25	47.76
TiO_2	(wt%)	0.94	1.05	0.87	1.00
Al_2O_3	(wt%)	14.38	15.75	14.21	15.99
FeO*	(wt%)	10.03	8.78	9.95	9.72
FeO	(wt%)	8.54	7.53	8.57	8.26
Fe_2O_3	(wt%)	1.66	1.39	1.53	1.62
MgO	(wt%)	12.52	11.04	12.56	12.11
MnO	(wt%)	0.16	0.15	0.16	0.16
CaO	(wt%)	11.31	11.83	11.02	10.45
Na_2O	(wt%)	1.87	2.13	1.80	2.56
K_2O	(wt%)	0.06	0.09	0.04	0.04
P_2O_5	(wt%)	0.10	0.12	0.09	0.10
S	(ppm)	1124.49		971.73	
Cl	(ppm)	143.39		78.41	
H_2O	(wt%)	0.24	0.30	0.14	0.32
$Fe^{3+}/\Sigma Fe$		0.149	0.143	0.138	0.150
F TiO_2		11%	9%	12%	10%
C^0_{H2O}		0.028	0.030	0.018	0.034
PAL	(%)	3.8%	3.7%	2.0%	4.4%
Afar Plume	(%)	29%	12%	10%	17%
DMM	(%)	68%	85%	88%	79%

Table 4 Cont.

Primary melt major elements and mantle component proportions

Sample		V3307 69D-1g	V3307 51D-1g	V3307 50D-1g
SiO_2	(wt%)	48.95	49.92	49.87
TiO_2	(wt%)	1.17	1.02	1.28
Al_2O_3	(wt%)	13.56	13.67	12.72
FeO*	(wt%)	10.37	9.87	10.31
FeO	(wt%)	8.92	8.01	8.80
Fe_2O_3	(wt%)	1.60	2.06	1.68
MgO	(wt%)	13.08	11.73	12.90
MnO	(wt%)	0.17	0.14	0.15
CaO	(wt%)	10.35	10.98	9.73
Na_2O	(wt%)	2.06	1.93	2.05
K_2O	(wt%)	0.04	0.40	0.63
P_2O_5	(wt%)	0.12	0.18	0.23
S	(ppm)		826.55	779.47
Cl	(ppm)		318.56	445.72
H_2O	(wt%)	0.14	0.51	0.74
$Fe^{3+}/\Sigma Fe$		0.139	0.188	0.146
F TiO_2		8%	9%	7%
C^0_{H2O}		0.012	0.053	0.058
PAL	(%)	4.5%	2.3%	6.9%
Afar Plume	(%)	17%	87%	100%
DMM	(%)	79%	11%	-6.6%

* = total Fe content reported as FeO

Table 5.

H_2O of each mantle component

	H_2O (wt%)
DMM*	0.012
Afar Plume	0.06
PAL	0-0.4

*DMM H_2O is from Kelley et al., 2006

References

Alain Burgisser; Marina Alletti; Bruno Scaillet (2015), "D-Compress," https://vhub.org/resources/3791.

Barberi, F., & Varet, J. (1970). The Erta Ale volcanic range (Danakil depression, northern afar, ethiopia). *Bulletin Volcanologique*, *34*(4), 848–917. https://doi.org/10.1007/BF02596805

Bastow, I. D., Nyblade, A. A., Stuart, G. W., Rooney, T. O., & Benoit, M. H. (2008). Upper mantle seismic structure beneath the Ethiopian hot spot: Rifting at the edge of the African low-velocity anomaly: ETHIOPIAN UPPER MANTLE SEISMIC STRUCTURE. *Geochemistry, Geophysics, Geosystems*, *9*(12), n/a-n/a. https://doi.org/10.1029/2008GC002107

Bosworth, W., Huchon, P., & McClay, K. (2005). The Red Sea and Gulf of Aden Basins. *Journal of African Earth Sciences*, *43*(1–3), 334–378. https://doi.org/10.1016/j.jafrearsci.2005.07.020

Brounce, M., Stolper, E., & Eiler, J. (2017). Redox variations in Mauna Kea lavas, the oxygen fugacity of the Hawaiian plume, and the role of volcanic gases in Earth's oxygenation. *Proceedings of the National Academy of Sciences*, *114*(34), 8997–9002. https://doi.org/10.1073/pnas.1619527114

Brounce, M., Stolper, E., & Eiler, J. (2022). The mantle source of basalts from Reunion Island is not more oxidized than the MORB source mantle. *Contributions to Mineralogy and Petrology*, *177*(1), 7. https://doi.org/10.1007/s00410-021-01870-w

Buck, W. Roger. (2004). Consequences of Asthenospheric Variability on Continental Rifting. *Rheology and Deformation of the Lithosphere at Continental Margins*, New York Chichester, West Sussex: Columbia University Press, pp. 1-30. https://doi.org/10.7312/karn12738-002

Burgisser, A., Alletti, M., & Scaillet, B. (2015). Simulating the behavior of volatiles belonging to the C–O–H–S system in silicate melts under magmatic conditions with the software D-Compress. *Computers & Geosciences*, *79*, 1–14. https://doi.org/10.1016/j.cageo.2015.03.002

Chorowicz, J. (2005). The East African rift system. *Journal of African Earth Sciences*, *43*(1–3), 379–410. https://doi.org/10.1016/j.jafrearsci.2005.07.019

Cochran, J. R. (1981). The Gulf of Aden: Structure and evolution of a young ocean basin and continental margin. *Journal of Geophysical Research*, *86*(B1), 263. https://doi.org/10.1029/JB086iB01p00263

Condie, K. C., & Kröner, A. (2008). When did plate tectonics begin? Evidence from the geologic record. In *Special Paper 440: When Did Plate Tectonics Begin on Planet Earth?* (Vol. 440, pp. 281–294). Geological Society of America. https://doi.org/10.1130/2008.2440(14)

Corti, G. (2012). Evolution and characteristics of continental rifting: Analog modeling-inspired view and comparison with examples from the East African Rift System. *Tectonophysics*, *522–523*, 1–33. https://doi.org/10.1016/j.tecto.2011.06.010

Cottrell, E., Lanzirotti, A., Mysen, B., Birner, S., Kelley, K. A., Botcharnikov, R., et al. (2018). A Mössbauer-based XANES calibration for hydrous basalt glasses reveals radiation-induced oxidation of Fe. *American Mineralogist*, *103*(4), 489–501. https://doi.org/10.2138/am-2018-6268

Dasgupta, R., & Hirschmann, M. M. (2007). Effect of variable carbonate concentration on the solidus of mantle peridotite. *American Mineralogist*, *92*(2–3), 370–379. https://doi.org/10.2138/am.2007.2201

Davies, J. H. (2013). Global map of solid Earth surface heat flow: Global Surface Heat Flow Map. *Geochemistry, Geophysics, Geosystems*, *14*(10), 4608–4622. https://doi.org/10.1002/ggge.20271

Donovan, A., Blundy, J., Oppenheimer, C., & Buisman, I. (2018). The 2011 eruption of Nabro volcano, Eritrea: perspectives on magmatic processes from melt inclusions. *Contributions to Mineralogy and Petrology*, *173*(1), 1. https://doi.org/10.1007/s00410-017-1425-2

Emry, E. L., Shen, Y., Nyblade, A. A., Flinders, A., & Bao, X. (2019). Upper Mantle Earth Structure in Africa From Full-Wave Ambient Noise Tomography. *Geochemistry, Geophysics, Geosystems*, *20*(1), 120–147. https://doi.org/10.1029/2018GC007804

Field, L., Blundy, J., Brooker, R. A., Wright, T., & Yirgu, G. (2012). Magma storage conditions beneath Dabbahu Volcano (Ethiopia) constrained by petrology, seismicity and satellite geodesy. *Bulletin of Volcanology*, *74*(5), 981–1004. https://doi.org/10.1007/s00445-012-0580-6

Field, Lorraine, Barnie, T., Blundy, J., Brooker, R. A., Keir, D., Lewi, E., & Saunders, K. (2012). Integrated field, satellite and petrological observations of the November 2010 eruption of Erta Ale. *Bull Volcanol*, 21.

Fleet, M. E. (2005). XANES SPECTROSCOPY OF SULFUR IN EARTH MATERIALS. *The Canadian Mineralogist*, *43*(6), 1811–1838. https://doi.org/10.2113/gscanmin.43.6.1811

Forsyth, D., & Uyeda, S. (1975). On the Relative Importance of the Driving Forces of Plate Motion. *Geophysical Journal International*, *43*(1), 163–200. https://doi.org/10.1111/j.1365-246X.1975.tb00631.x

Gallacher, R. J., Keir, D., Harmon, N., Stuart, G., Leroy, S., Hammond, J. O. S., et al. (2016). The initiation of segmented buoyancy-driven melting during continental breakup. *Nature Communications*, *7*(1), 13110. https://doi.org/10.1038/ncomms13110

Gualda, G. A. R., & Ghiorso, M. S. (2015). MELTS_Excel: AMicrosoft Excel-based MELTS interface for research and teaching of magma properties and evolution. *Geochemistry, Geophysics, Geosystems*, *16*(1), 315–324. https://doi.org/10.1002/2014GC005545

Hofmann, C., Courtillot, V., Féraud, G., Rochette, P., Yirgu, G., Ketefo, E., & Pik, R. (1997). Timing of the Ethiopian flood basalt event and implications for plume birth and global change. *Nature*, *389*(6653), 838–841. https://doi.org/10.1038/39853

Jaupart, C. (2009). Heat Flow and Thermal Structure of the Lithosphere. In *Treatise on Geophysics* (1st Edition, Vol. 6, pp. 218–246).

Jenner, F. E., & O'Neill, H. St. C. (2012). Analysis of 60 elements in 616 ocean floor basaltic glasses: TECHNICAL BRIEF. *Geochemistry, Geophysics, Geosystems*, *13*(2), n/a-n/a. https://doi.org/10.1029/2011GC004009

Jugo, P. J. (2009). Sulfur content at sulfide saturation in oxidized magmas. *Geology*, *37*(5), 415–418. https://doi.org/10.1130/G25527A.1

Karato, S., & Jung, H. (1998). Water, partial melting and the origin of the seismic low velocity and high attenuation zone in the upper mantle. *Earth and Planetary Science Letters*, *157*(3–4), 193–207. https://doi.org/10.1016/S0012-821X(98)00034-X

Karato, S.-I., & Jung, H. (2003). Effects of pressure on high-temperature dislocation creep in olivine. *Philosophical Magazine*, *83*(3), 401–414. https://doi.org/10.1080/0141861021000025829

Kelley, K. A., Plank, T., Grove, T. L., Stolper, E. M., Newman, S., & Hauri, E. (2006). Mantle melting as a function of water content beneath back-arc basins. *Journal of Geophysical Research*, *111*(B9), B09208. https://doi.org/10.1029/2005JB003732

Kelley, K. A., Kingsley, R., & Schilling, J.-G. (2013). Composition of plume-influenced mid-ocean ridge lavas and glasses from the Mid-Atlantic Ridge, East Pacific Rise, Galápagos Spreading Center, and Gulf of Aden: PLUME-INFLUENCED MORB. *Geochemistry, Geophysics, Geosystems*, *14*(1), 223–242. https://doi.org/10.1002/ggge.20049

Kress, V. C., & Carmichael, I. S. E. (n.d.). The compressibility of silicate liquids containing Fe203 and the effect of composition, temperature, oxygen fugacity and pressure on their redox states, 11.

Kress, V. C., & Ghiorso, M. S. (2004). Thermodynamic modeling of post-entrapment crystallization in igneous phases. *Journal of Volcanology and Geothermal Research*, *137*(4), 247–260. https://doi.org/10.1016/j.jvolgeores.2004.05.012

Mohr, P., & Zanettin, B. (1988). The Ethiopian Flood Basalt Province. In J. D. Macdougall (Ed.), *Continental Flood Basalts* (Vol. 3, pp. 63–110). Dordrecht: Springer Netherlands. https://doi.org/10.1007/978-94-015-7805-9_3

de Moor, J. M., Fischer, T. P., Sharp, Z. D., King, P. L., Wilke, M., Botcharnikov, R. E., et al. (2013). Sulfur degassing at Erta Ale (Ethiopia) and Masaya (Nicaragua) volcanoes: Implications for degassing processes and oxygen fugacities of basaltic systems: Sulfur Degassing at Basaltic Volcanoes. *Geochemistry, Geophysics, Geosystems*, *14*(10), 4076–4108. https://doi.org/10.1002/ggge.20255

Moore, C., Wright, T., Hooper, A., & Biggs, J. (2019). The 2017 Eruption of Erta 'Ale Volcano, Ethiopia: Insights Into the Shallow Axial Plumbing System of an Incipient Mid-Ocean Ridge. *Geochemistry, Geophysics, Geosystems*, *20*(12), 5727–5743. https://doi.org/10.1029/2019GC008692

Muth, M. J., & Wallace, P. J. (2021). Slab-derived sulfate generates oxidized basaltic magmas in the southern Cascade arc (California, USA). *Geology*, *49*(10), 1177–1181. https://doi.org/10.1130/G48759.1

Nash, W. M., Smythe, D. J., & Wood, B. J. (2019). Compositional and temperature effects on sulfur speciation and solubility in silicate melts. *Earth and Planetary Science Letters*, *507*, 187–198. https://doi.org/10.1016/j.epsl.2018.12.006

Newman, S., & Lowenstern, J. B. (2002). VolatileCalc: a silicate melt–H2O–CO2 solution model written in Visual Basic for excel. *Computers & Geosciences*, *28*(5), 597–604. https://doi.org/10.1016/S0098-3004(01)00081-4

Nicklas, R. W., Hahn, R. K. M., & Day, J. M. D. (2022). Oxidation of La Réunion lavas with MORB-like fO2 by assimilation. *Geochemical Perspectives Letters*, *20*, 32–36. https://doi.org/10.7185/geochemlet.2205

Pasyanos, M. E. (2010). Lithospheric thickness modeled from long-period surface wave dispersion. *Tectonophysics*, *481*(1–4), 38–50. https://doi.org/10.1016/j.tecto.2009.02.023

Plank, T., Kelley, K. A., Zimmer, M. M., Hauri, E. H., & Wallace, P. J. (2013). Why do mafic arc magmas contain ~4wt% water on average? *Earth and Planetary Science Letters*, *364*, 168–179. https://doi.org/10.1016/j.epsl.2012.11.044

Putirka, K. (1999). Clinopyroxene + liquid equilibria to 100 kbar and 2450 K. *Contributions to Mineralogy and Petrology*, *135*(2–3), 151–163. https://doi.org/10.1007/s004100050503

Ravel, B. & Newville, M. (2005). J. Synchrotron Rad. 12, 537-541.

Roeder, P. L., & Emslie, R. F. (1970). Olivine-liquid equilibrium. *Contributions to Mineralogy and Petrology*, *29*(4), 275–289. https://doi.org/10.1007/BF00371276

Rooney, T. O., Herzberg, C., & Bastow, I. D. (2012). Elevated mantle temperature beneath East Africa. *Geology*, *40*(1), 27–30. https://doi.org/10.1130/G32382.1

Rooney, Tyrone O., Hanan, B. B., Graham, D. W., Furman, T., Blichert-Toft, J., & Schilling, J.-G. (2012). Upper Mantle Pollution during Afar Plume–Continental Rift Interaction. *Journal of Petrology*, *53*(2), 365–389. https://doi.org/10.1093/petrology/egr065

Saal, A. E., Hauri, E. H., Langmuir, C. H., & Perfit, M. R. (2002). Vapour undersaturation in primitive mid-ocean-ridge basalt and the volatile content of Earth's upper mantle. *Nature*, *419*(6906), 451–455. https://doi.org/10.1038/nature01073

Schaeffer, A. J., & Lebedev, S. (2013). Global shear speed structure of the upper mantle and transition zone. *Geophysical Journal International*, *194*(1), 417–449. https://doi.org/10.1093/gji/ggt095

Schilling, J.-G., Kingsley, R. H., Hanan, B. B., & McCully, B. L. (1992). Nd-Sr-Pb isotopic variations along the Gulf of Aden: Evidence for Afar Mantle Plume-Continental Lithosphere Interaction. *Journal of Geophysical Research*, *97*(B7), 10927. https://doi.org/10.1029/92JB00415

Scoon, R. N. (2018). The East African Rift System. In R. N. Scoon, *Geology of National Parks of Central/Southern Kenya and Northern Tanzania* (pp. 19–28). Cham: Springer International Publishing. https://doi.org/10.1007/978-3-319-73785-0_3

Spampinato, L., Oppenheimer, C., Calvari, S., Cannata, A., & Montalto, P. (2008). Lava lake surface characterization by thermal imaging: Erta 'Ale volcano (Ethiopia): THERMAL IMAGING OF ERTA 'ALE LAVA LAKE. *Geochemistry, Geophysics, Geosystems*, *9*(12), n/a-n/a. https://doi.org/10.1029/2008GC002164

Till, C. B., Grove, T. L., & Withers, A. C. (2012). The beginnings of hydrous mantle wedge melting. *Contributions to Mineralogy and Petrology*, *163*(4), 669–688. https://doi.org/10.1007/s00410-011-0692-6

Zelenski, M. E., Fischer, T. P., de Moor, J. M., Marty, B., Zimmermann, L., Ayalew, D., et al. (2013). Trace elements in the gas emissions from the Erta Ale volcano, Afar, Ethiopia. *Chemical Geology*, *357*, 95–116. https://doi.org/10.1016/j.chemgeo.2013.08.022